ORIGINAL ARTICLE

Bi-directional thermal buckling and resonance frequency characteristics of a GNP-reinforced composite nanostructure

Jing Li[1] · Fei Tang[1] · Mostafa Habibi[2,3]

Abstract

In this article, thermal buckling and resonance frequency of a composite cylindrical nanoshell reinforced with graphene nanoplatelets (GNP) under bi-directional thermal loading are presented. The temperature-dependent material properties of piece-wise GNP-reinforced composites (GNPRC) are assumed to be graded in the thickness direction of a cylindrical nanoshell. Also, Halphin-Tsai nanomechanical model is used to surmise the effective material properties of each layer. The size-dependent GNPRC nanoshell is analyzed using modified couple stress parameter (FMCS). For the first time, in the presented study show that bi-directional thermal buckling occurs if the percent of relative frequency change tends to 30%. The novelty of the current study is in considering the effects of bi-directional thermal loading in addition of FMCS on relative frequency, resonance frequencies, thermal buckling, and dynamic deflection of the GNPRC nanoshell. The governing equations and boundary conditions are developed using Hamilton's principle and solved with the aid of analytical method. The results show that, various bi-directionasl thermal loading and other geometrical and mechanical properties have important role on resonance frequency, relative frequency change, thermal buckling, and dynamic deflection of the GNPRC cylindrical nanoshell. The results of the current study are useful suggestions for design of materials science, micro-mechanical and nano-mechanical systems such as microactuators and microsensors.

Keywords Bi-directional thermal loading · Resonance frequency · Graphene nanoplatelet · Thermal buckling · FMCS

1 Introduction

According to the recent progressions in science and technology [1–8], novel and new research aspects have considerable attention [9–17]. Some applications of GPL reinforcement are reported in Ref. [18]. In addition, the properties of GPL reinforcements make them an appropriate choice to be used in chemistry, physics, electrical engineering, materials science [19] and engineering applications [20–29].

Rafiee et al. [30] compared the mechanical properties of epoxy nanocomposites refined with 1% value fraction of single-walled carbon nanotubes (SWNT), multi-walled carbon nanotube (MWNT) and GPL with each other. Their results show that, Young's modulus, ultimate tensile strength, fracture toughness, fracture energy, and fatigue resistance of the GPLs are greater than the other materials. So, GPL reinforcement can be replaced by SWNTs and MWNTs in many applications (Fig. 1).

In addition, Yavari et al. [31] reported microstructure of epoxy/GNP nanocomposites. The grains with the Brighter background is epoxy and the bounded which reinforcement the epoxy is GNP (Fig. 2).

Researches demonstrated that subjoining very meager amount of graphene into primary polymer matrix can desperately improve its mechanical, thermal and electrical properties. It is worth to mention that nanostructures reinforced by GPL are more applicable in engineering design, so focus on dynamic modeling of the nanostructure with

✉ Jing Li
lj_mais@126.com

✉ Mostafa Habibi
mostafahabibi@duytan.edu.vn

Fei Tang
Tang_but@126.com

1 School of Urban Construction, Wuchang University of Technology, Wuhan 430223, China

2 Institute of Research and Development, Duy Tan University, Da Nang 550000, Vietnam

3 Faculty of Electrical–Electronic Engineering, Duy Tan University, Da Nang 550000, Vietnam

Fig. 1 Ultimate tensile strength and Young modulus for the baseline epoxy and GNP/epoxy, MWNT/epoxy, and SWNT/epoxy nanocomposites [30]
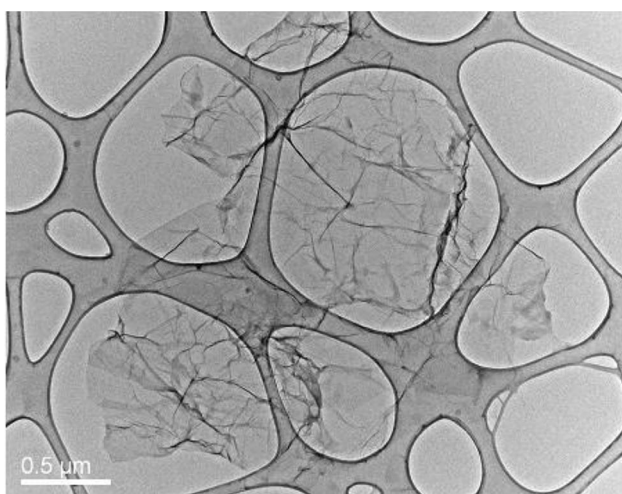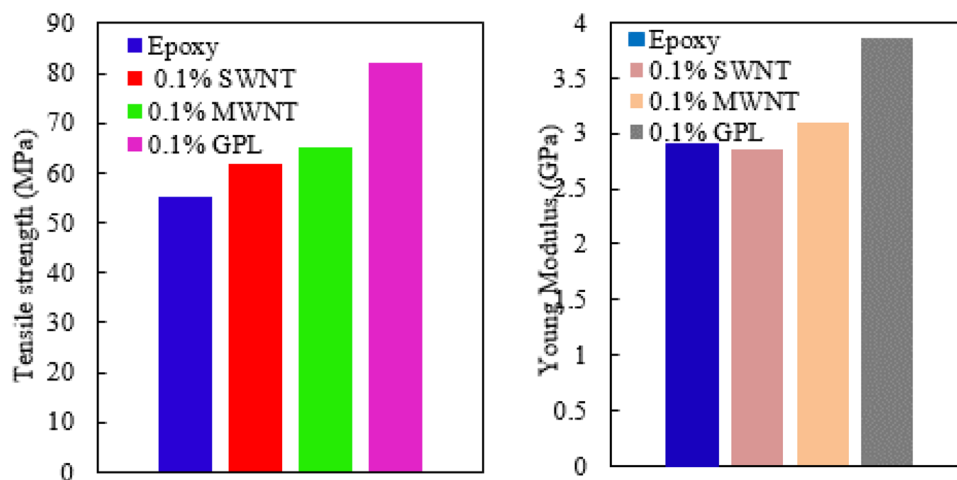

Fig. 2 Microstructure of epoxy nanocomposites refined with GNP [31]

GPL reinforcement is useful and important. In addition, this material can be used in electrical devices such as those mentioned in Refs. [32–35]. Furthermore, polymer matrix reinforced by various types of nanofillers has a wide range of applications such as field effect transistors, electromechanical actuators, biosensors and chemical sensors, solar cells, photoconductor and superconductor devices. Therefore, investigation of their mechanical characteristics is of great interest for engineering design and manufacture. Many researchers [36–41] studied the behavior and stability of the FG multilayer composite and isotropic materials. Feg et al. [42] investigated nonlinear bending behavior of a novel glass made of multi-layer polymer composite beams reinforced by GPLs. They reported that beams with a high weight fraction of GPLs and symmetric distribution are less sensitive to the nonlinear deformation. In addition, current nanostructure can be used in smart systems. The experiments and researches show that size effects play an important role

in mechanical properties. Thus, neglecting these effects may lead to inaccurate responses. It should be mentioned that, the size effect is not considered in the classical continuum theories, so these theories are not appropriate for micro and nano scales. Therefore, some methods, such as: molecular dynamic (MD) simulations, FE method and non-classical continuum theory are used to study nanostructures. MD simulation includes complicated and time-consuming calculations which are not efficient. In contrast, simple and efficient, higher order continuum mechanic theories, have recently attracted researcher's attentions. As studying the mechanical behaviors of nanoshells relate to submicron dimensions, they could not be correctly predicted by the classical theory. Thus taking into consideration the size effect, higher order continuum theories are used. These theories include the nonlocal elasticity theory, the modified couple stress theory, and nonlocal strain gradient theory. A Bernoulli–Euler nanobeam model considering nonhomogeneous temperature fields, based on Eringen's nonlocal elasticity theory was proposed by Ref. [43]. They presented a thermodynamically consistent and reliable nonlocal nanobeam model that can be used in non-homogenous and non-isothermal environments. Bending analysis of armchair carbon nanotubes using gradient elasticity theory was examined by Ref. [44]. In this article, as an important result, influences of small-size effects on the Young's modulus were investigated. Exact solutions of inflected functionally graded nanobeams with integral elasticity were investigated by Ref. [45]. The solutions of the stress-driven integral method indicate that the stiffness of nanobeams increases at smaller scales due to size effects.

A key issue in various engineering field is that the prediction of the properties, behavior, and performance of different systems is an important aspect [46–55]. For this regard, in field of the dynamic/static responses of the size-dependent GPLRC nanostructures, sahmani et al. [56] studied nonlinear instability of GPLRC nanoshells under the hydrostatic pressure using nonlocal elasticity theory and MSGT. In another

work [57], they investigated nonlinear instability of axially loaded GPLRC nanoshells based on nonlocal strain gradient elasticity theory. It should be noted that, MSGT is an high order continuum theory which employs three length scale parameters [58]. These parameters are very useful in modeling of nano structures which are introduced in results section. In addition, in the field of forced vibration analysis of structures, Song et al. [59] investigated free and forced vibration of FG polymer composite plates reinforced by GPLs. They studied the effects of GPL distribution pattern, weight function, geometry and size, as well as, the total number of layers on the dynamic characteristics of the plates. Forced vibration of an orthotropic double-nanoplate system using nonlocal theory was examined by Atanasov et al. [60]. In their research, employing an analytical method the dynamic responses of the orthotropic double-nanoplate system for different external transversal loads were studied. Also, Du et al. [61] investigated nonlinear forced vibration of infinitely long FG cylindrical shells using the Lagrangian theory and multiple scale method. An interesting result of their work is that, power-law exponents have important role on the amplitude response of the FG cylindrical shells. Li et al. [62] focused on the coupled vibration characteristics of a spinning and axially moving composite thin-walled beam. In their work, some interesting conclusions about the critical axial speed and critical spinning angular speed were drawn. Another important factor in the design of composite nanostructures is porosity which occurs during manufacturing process. Therefore, these phenomena must be considered in the simulation and modeling of nanostructures. Barati et al. [63] studied forced vibration analysis of heterogeneous nanoporous plates using generalized nonlocal strain gradient theory. They showed that the forced vibration characteristics of a nanoplate are strongly influenced by the excitation frequency, porosities, nonlocal parameter and dynamic load location. Free and forced vibration characteristics of FG porous beams with non-uniform porosity distribution were studied by Chen et al. [64]. They examined both symmetric and asymmetric porosity distributions in this work. Chen et al. [65] conducted a study on nonlinear free vibration behavior of a porous moderately thick beam. They used Ritz method and von Kármán type nonlinear strain–displacement relations for deriving the equation system. According to their results, porosity coefficient, slenderness ratio, thickness ratio and other parameters play important roles in the nonlinear vibration characteristics of the porous moderately thick beam. In another work, Chen et al. [66] examined nonlinear vibration and post-buckling behaviors of GPLRC porous nanocomposite beam. Moreover, the influences of both porosity coefficient and GPL weight fraction on static and dynamic behaviors of the GPLRC porous nanocomposite were shown in their work. Y.H. Dong et al. [67] studied free vibration characteristics of a GPLRC porous nanocomposite cylindrical shell with spinning motion. Finally, they represented the effect of initial hoop tension on vibration characteristics of the spinning GPLRC porous nanocomposite cylindrical shell. Yang et al. [68] investigated buckling and free vibration characteristics of GPLRC nanocomposite plates with porosity. Recently, Chen et al. [69] focused on dynamic response and energy absorption of FG two-dimensional porous structures in the framework of finite element analysis. Li et al. [70] investigated free vibration characteristics of a spinning composite thin-walled beam under the hydrothermal environment. Their governing equations and boundary conditions were solved using Galerkin's method. In their result, the effects of spinning motion and hydrothermal environment on natural frequency and critical spinning angular speed of the beam were examined. In another work, Li et al. [71] investigated parametric instability of a FG cylindrical thin shell under the thermal environment. In other work [72], they studied parametric resonance of a FG cylindrical thin shell with periodic rotating angular speeds in the thermal environment. They also demonstrated that constant of rotating angular speed, material heterogeneity and thermal effects have remarkable influence on vibration characteristics, instability regions and critical rotating speeds of the shell. Nonlinear vibration of FG cylindrical shells in thermal environments was studied by Ref. [73]. Du et al. [74] analyzed nonlinear vibration of FG circular cylindrical shells in thermal environment. Their results showed that, temperature and volume fractions of composition play an important role in the exact resonance condition and bifurcation characteristics of FG cylindrical shells. Also, some researchers tried to predict the static and dynamic properties of different structures and materials via neural network solution [75–89].

To the best of our knowledge, no studies have been reported in the literature for investigation of bi-directional thermal buckling using relative frequency changes. For the first time, in the present study show that bi-directional thermal buckling occurs if the percent of relative frequency change tends to 30%. The novelty of the current study is consideration of GNPRC, bi-directional, thermal loading, dynamic load and size effects implemented on proposed model using FMCS. Because of high accuracy and efficiency of the analytical method, it is employed to solve the governing equations of the problem. The governing equations and boundary conditions have been developed using minimum potential energy which solved with the aid of the analytical method. Finally, using the mentioned continuum mechanics theory, the investigation has been made into the influence of the bi-directional thermal loading and GNP distribution pattern on the thermal buckling, resonance frequency, relative frequency change and dynamic deflection.

2 Multilayer polymer composites reinforced GNPs formulation

A cylindrical nanoshell in bi-directional thermal environment and under dynamic load is modeled. The thickness, length, and the middle surface radius of the cylindrical shell are denoted by h, L, and R, respectively. In addition, q_0 is the transverse force due to applied dynamic load (Fig. 3).

The cylindrical nanoshell is made of composite material. The volume fraction functions of these four patterns of GPL are represented by [90, 91]

$$\text{Pattern 1}:\ U - GPLRC\,(UD):\quad V_{GPL}(k) = V_{GPL}^* \tag{1}$$

$$\text{Pattern 2}:\ X - GPLRC\,(FG - X):$$
$$V_{GPL}(k) = 2V_{GPL}^*\big|2k - N_L - 1\big|/N_L \tag{2}$$

$$\text{Pattern 3}:\ O - GPLRC\,(FG - O):$$
$$V_{GPL}(k) = 2V_{GPL}^*\big[1 - \big(|2k - N_L - 1|/N_L\big)\big] \tag{3}$$

$$\text{Pattern 4}:\ A - GPLRC\,(FG - A):\quad V_{GPL}(k) = 2V_{GPL}^*(2k - 1)/N_L \tag{4}$$

where k is number of layers of the nanoshell, N_L is the total number of layers and V_{GPL}^* is the total volume fraction of GNPs. The relation between V_{GPL}^* and their weight fraction g_{GPL} can be expressed by [92–97]:

$$V_{GPL}^* = \frac{g_{GPL}}{g_{GPL} + (\rho_{GPL}/\rho_m)(1 - g_{GPL})} \tag{5}$$

in which ρ_{GPL} and ρ_m are the mass densities of GNPs and the polymer matrix. Based on Halpin–Tsai model, the elastic modulus of composites reinforced randomly with GNPs approximated by [98–100]:

$$E = \frac{3}{8}E_L + \frac{5}{8}E_T,$$
$$E_L = \frac{1 + \xi_L n_L V_{GPL}}{1 - n_L V_{GPL}}E_m,\quad E_T = \frac{1 + \xi_T n_T V_{GPL}}{1 - n_T V_{GPL}}E_m \tag{6}$$

where E is effective modulus of composites reinforced with GNPs and E_L and E_T are the longitudinal and transverse module for a unidirectional lamina. In Eq. (6) the GNP geometry factors (ξ_L and ξ_T) and other parameters are given by [101, 102]:

$$\xi_L = 2(\mathbb{Z}_{GPL}/h_{GPL}),\quad \xi_t = 2(b_{GPL}/h_{GPL}),$$
$$n_L = \frac{(E_{GPL}/E_m) - 1}{(E_{GPL}/E_m) + \xi_L},\quad n_T = \frac{(E_{GPL}/E_m) - 1}{(E_{GPL}/E_m) + \xi_T} \tag{7}$$

where $\mathbb{Z}_{GPL}\mathbb{Z}_{GPL}, h_{GPL}, b_{GPL}$ are the average length, thickness and width of the GNPs. Using rule of mixture, mechanical properties of the GNP/ polymer nanocomposite are expressed as [103]:

$$\overline{E} = E_{GPL}V_{GPL} + E_M V_M,$$
$$\overline{\rho} = \rho_{GPL}V_{GPL} + \rho_M V_M,$$
$$\overline{\nu} = \nu_{GPL}V_{GPL} + \nu_M V_M,$$
$$\overline{\alpha} = \alpha_{GPL}V_{GPL} + \alpha_M V_M. \tag{8}$$

The mechanical properties of the FG-GNPR cylindrical shell with different types of distributions can be obtained by [104]:

3 Mathematical modelling

Based on the first order shear deformation theory [105] (FSDT), the displacement field of cylindrical shell along the three directions of x, θ, z is as follows:

$$u(x, \theta, z, t) = u_0(x, \theta, t) + z\psi_x(x, \theta, t)$$
$$v(x, \theta, z, t) = v_0(x, \theta, t) + z\psi_\theta(x, \theta, t)$$
$$w(x, \theta, z, t) = w_0(x, \theta, t) \tag{9}$$

where, $u_0(x, \theta, z), v_0(x, \theta, z)$ and $w_0(x, \theta, z)$) represent the displacements in axial-, circumferential- and radial-directions, respectively. $\psi_x(x, \theta, t)$ and $\psi_\theta(x, \theta, t)$ are the rotations of the normal to the element middle plane about the circumferential and axial-directions. In addition, the three-dimensional stress–strain relations can be expressed as follows [106–109]:

$$
\begin{bmatrix}
\sigma_{xx} \\
\sigma_{\theta\theta} \\
\sigma_{zz} \\
\sigma_{x\theta} \\
\sigma_{xz} \\
\sigma_{\theta z}
\end{bmatrix}
=
\begin{bmatrix}
\overline{Q}_{11} & \overline{Q}_{12} & \overline{Q}_{13} & 0 & 0 & 0 \\
\overline{Q}_{12} & \overline{Q}_{22} & \overline{Q}_{23} & 0 & 0 & 0 \\
\overline{Q}_{13} & \overline{Q}_{23} & \overline{Q}_{33} & 0 & 0 & 0 \\
0 & 0 & 0 & \overline{Q}_{44} & 0 & 0 \\
0 & 0 & 0 & 0 & \overline{Q}_{55} & 0 \\
0 & 0 & 0 & 0 & 0 & \overline{Q}_{66}
\end{bmatrix}
\begin{bmatrix}
\varepsilon_{xx} \\
\varepsilon_{\theta\theta} \\
\varepsilon_{zz} \\
\varepsilon_{x\theta} \\
\varepsilon_{xz} \\
\varepsilon_{\theta z}
\end{bmatrix}
\tag{10}
$$

In Eq. (10) the stiffness coefficients are obtained by Ref. [110–112]. Also, α_i and ΔT are thermal expansions (in x, θ and z directions) and temperature changes, respectively. For the equations of the motion and boundary conditions, the extended Hamilton's principle states that [113–117]:

$$\int_{t_1}^{t_2} (\delta T - \delta U + \delta W_1 - \delta W_2)dt = 0 \tag{11}$$

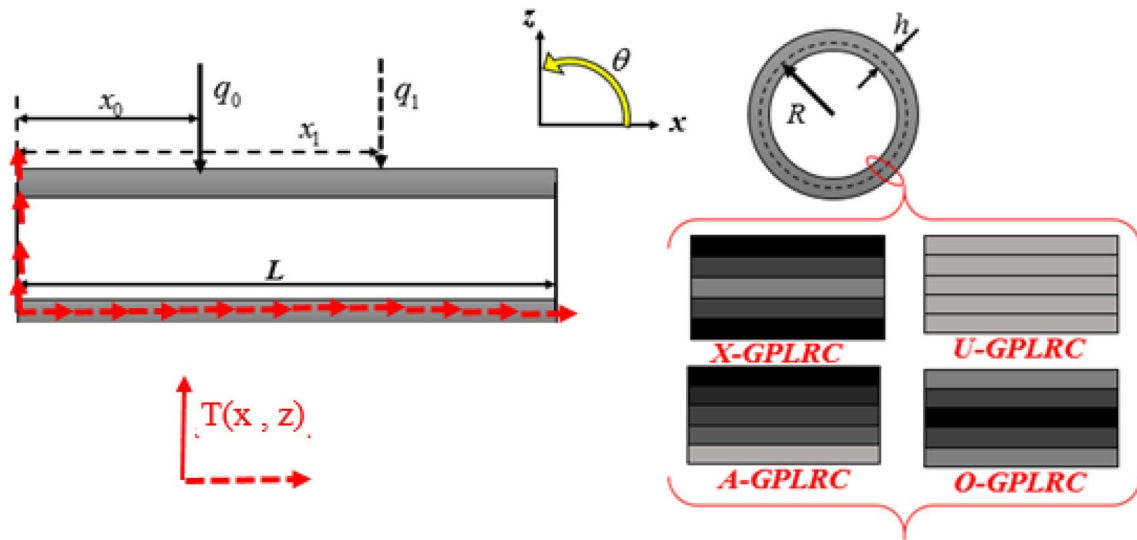Strain energy of FMCS parameter cylindrical nanoshell is expressed as follows [118, 119]:

Fig. 3 Geometry of cylindrical FG nanoshell under dynamic load and thermal environment

$$U = \frac{1}{2} \iiint\limits_{V} (\sigma_{ij}\varepsilon_{ij} + m_{ij}^{s}\chi_{ij}^{s})R\,dxd\theta dz \tag{12}$$

In Eq. (12) ε_{ij} and σ_{ij} represent the components of a strain tensor and stress tensor, which are expressed in Ref. [110]. In addition, χ_{ij}^{s} and m_{ij} are the components of a symmetric rotation gradient tensor and higher order stress tensor, which can be expressed as:

$$\chi_{ij}^{s} = \frac{1}{2}(\varphi_{i,j} + \varphi_{j,i})$$
$$m_{ij}^{s} = 2l^{2}\mu\chi_{ij}^{s} \tag{13}$$

where φ_{i} and ll respectively represent the extremely small rotation vector and MCS parameter, which is related to symmetric rotation gradients can be expressed as follows:

$$l = l_{GPL}V_{GPL} + l_{M}V_{M} \tag{14}$$

Moreover, the non-zero components of symmetric rotation gradient tensor are obtained as follows:

$$\chi_{xx}^{s} = -\frac{1}{2}\left(\frac{\partial\psi_{\theta}}{\partial x} + \frac{1}{R}\frac{\partial v}{\partial x} - \frac{1}{R}\frac{\partial^{2}w}{\partial x\partial\theta}\right)$$

$$\chi_{\theta\theta}^{s} = -\frac{1}{2R}\left(\frac{1}{R}\frac{\partial u}{\partial\theta} - \frac{\partial v}{\partial x} - z\frac{\partial\psi_{\theta}}{\partial x}\right) - \frac{1}{2}\left(\frac{1}{R}\frac{\partial^{2}w}{\partial x\partial\theta} - \frac{1}{R}\frac{\partial\psi_{x}}{\partial\theta}\right)$$

$$\chi_{zz}^{s} = -\frac{1}{2}\left(\frac{1}{R}\frac{\partial\psi_{x}}{\partial\theta} - \frac{\partial\psi_{\theta}}{\partial x} - \frac{1}{R^{2}}\frac{\partial u}{\partial\theta}\right)$$

$$\chi_{x\theta}^{s} = -\frac{1}{4}\left(\frac{1}{R^{2}}\frac{\partial v}{\partial\theta} + \frac{\partial^{2}w}{\partial x^{2}} - \frac{1}{R^{2}}\frac{\partial^{2}w}{\partial\theta^{2}} - \frac{\partial\psi_{x}}{\partial x} + \frac{1}{R}\frac{\partial\psi_{\theta}}{\partial\theta}\right)$$

$$\chi_{xz}^{s} = -\frac{1}{4}\left(\frac{1}{R}\frac{\partial^{2}u}{\partial x\partial\theta} - \frac{\partial^{2}v}{\partial x^{2}} - \frac{v}{R^{2}} + \frac{1}{R^{2}}\frac{\partial w}{\partial\theta} + \frac{\psi_{\theta}}{R}\right) - \frac{z}{4}\left(\frac{1}{R}\frac{\partial^{2}\psi_{\theta}}{\partial x\partial\theta} - \frac{\partial^{2}\psi_{\theta}}{\partial x^{2}}\right)$$

$$\chi_{\theta z}^{s} = -\frac{1}{4}\left(\frac{1}{R^{2}}\frac{\partial^{2}u}{\partial\theta^{2}} - \frac{1}{R}\frac{\partial^{2}v}{\partial x\partial\theta} - \frac{1}{R}\frac{\partial w}{\partial x} + \frac{\psi_{x}}{R}\right) - \frac{z}{4}\left(\frac{1}{R^{2}}\frac{\partial^{2}\psi_{x}}{\partial\theta^{2}} - \frac{1}{R}\frac{\partial^{2}\psi_{\theta}}{\partial x\partial\theta}\right) \tag{15}$$

Finally, the classical and non-classical strain energies of the current study based on FMCS parameter are expressed as follows:

$$\frac{1}{2}\iiint\limits_{V}(\sigma_{ij}\delta\varepsilon_{ij})dV = \iint\limits_{A}\left\{\begin{array}{l} \left(N_{xx}\frac{\partial}{\partial x}\delta u + M_{xx}\frac{\partial}{\partial x}\delta\psi_{x}\right) + N_{\theta\theta}\left(\frac{1}{R}\frac{\partial}{\partial\theta}\delta v + \frac{\delta w}{R}\right) + \\ M_{\theta\theta}\frac{1}{R}\frac{\partial}{\partial\theta}\delta\psi_{\theta} + Q_{xz}\left(\delta\psi_{x} + \frac{\partial}{\partial x}\delta w\right) + \\ N_{x\theta}\left(\frac{1}{R}\frac{\partial}{\partial\theta}\delta u + \frac{\partial}{\partial x}\delta v\right) + M_{x\theta}\left(\frac{1}{R}\frac{\partial}{\partial\theta}\delta\psi_{x} + \frac{\partial}{\partial x}\delta\psi_{\theta}\right) \\ + Q_{z\theta}\left(\delta\psi_{\theta} + \frac{1}{R}\frac{\partial}{\partial\theta}\delta w - \frac{\delta v}{R}\right) \end{array}\right\} Rdxd\theta$$

$$\frac{1}{2}\iiint\limits_{V}(m_{ij}^{s}\delta\chi_{ij}^{s})dV = \iint\limits_{A}\left\{\begin{array}{l} \left(-\frac{Y_{\theta\theta}}{2R^{2}} + \frac{Y_{zz}}{2R^{2}}\right)\frac{\partial}{\partial\theta}\delta u - \left(\frac{Y_{\theta z}}{2R^{2}}\right)\frac{\partial^{2}}{\partial\theta^{2}}\delta u \\ -\left(\frac{Y_{zx}}{2R}\right)\frac{\partial^{2}}{\partial\theta\partial x}\delta u \\ +\left(\frac{Y_{\theta\theta}}{2R} - \frac{Y_{xx}}{2R}\right)\frac{\partial}{\partial x}\delta v + \left(\frac{Y_{xz}}{2}\right)\frac{\partial^{2}}{\partial x^{2}}\delta v \\ -\left(\frac{Y_{\theta x}}{2R^{2}}\right)\frac{\partial}{\partial\theta}\delta v \\ +\left(\frac{Y_{\theta z}}{2R}\right)\frac{\partial^{2}}{\partial\theta\partial x}\delta v + \left(\frac{Y_{xz}}{2R^{2}}\right)\delta v + \left(\frac{Y_{\theta z}}{2R}\right)\frac{\partial}{\partial x}\delta w \\ -\left(\frac{Y_{\theta x}}{2}\right)\frac{\partial^{2}}{\partial x^{2}}\delta w \\ -\left(\frac{Y_{zx}}{2R^{2}}\right)\frac{\partial}{\partial\theta}\delta w + \left(\frac{Y_{x\theta}}{2R^{2}}\right)\frac{\partial^{2}}{\partial\theta^{2}}\delta w + \\ \left(-\frac{Y_{\theta\theta}}{2R} + \frac{Y_{xx}}{2R}\right)\frac{\partial^{2}}{\partial\theta\partial x}\delta w \\ +\left(\frac{Y_{x\theta}}{2}\right)\frac{\partial}{\partial x}\delta\psi_{x} + \left(\frac{Y_{\theta\theta}}{2R} - \frac{Y_{xx}}{2R}\right)\frac{\partial}{\partial\theta}\delta\psi_{x} \\ -\left(\frac{T_{zx}}{2R}\right)\frac{\partial^{2}}{\partial\theta\partial x}\delta\psi_{x} \\ -\left(\frac{Y_{z\theta}}{2R}\right)\delta\psi_{x} - \left(\frac{Y_{x\theta}}{2R}\right)\frac{\partial}{\partial\theta}\delta\psi_{\theta} + \\ \left(\frac{Y_{\theta\theta}}{2R} - \frac{Y_{xx}}{2} + \frac{Y_{zz}}{2}\right)\frac{\partial}{\partial x}\delta\psi_{\theta} \\ +\left(\frac{T_{z\theta}}{2R}\right)\frac{\partial^{2}}{\partial\theta\partial x}\delta\psi_{\theta} - \left(\frac{T_{z\theta}}{2R^{2}}\right)\frac{\partial^{2}}{\partial\theta^{2}}\delta\psi_{x} \\ +\left(\frac{T_{xz}}{2}\right)\frac{\partial^{2}}{\partial x^{2}}\delta\psi_{\theta} - \left(\frac{Y_{xz}}{2R}\right)\delta\psi_{\theta} \end{array}\right\} Rdxd\theta \tag{16}$$

where parameters used in above equation are defined as:

$$(N_{xx}, N_{\theta\theta}, N_{x\theta}) = \int_{-h/2}^{h/2} (\sigma_{xx}, \sigma_{\theta\theta}, \sigma_{x\theta}) dz,$$

$$(M_{xx}, M_{\theta\theta}, M_{x\theta}) = \int_{-h/2}^{h/2} (\sigma_{xx}, \sigma_{\theta\theta}, \sigma_{x\theta}) z dz,$$

$$(Q_{xz}, Q_{z\theta}) = \int_{-h/2}^{h/2} k_s (\sigma_{xz}, \sigma_{z\theta}) dz,$$

$$(Y_{xx}, Y_{\theta\theta}, Y_{zz}, Y_{x\theta}, Y_{xz}, Y_{\theta z}) = \int_{-h/2}^{h/2} (m_{xx}, m_{\theta\theta}, m_{zz}, m_{x\theta}, m_{xz}, m_{z\theta}) dz,$$

$$(T_{xx}, T_{\theta\theta}, T_{zz}, T_{x\theta}, T_{xz}, T_{z\theta}) = \int_{-h/2}^{h/2} (m_{xx}, m_{\theta\theta}, m_{zz}, m_{x\theta}, m_{xz}, m_{z\theta}) z dz$$

$$(17)$$

Furthermore, the kinetic energy of the FG-GRCs cylindrical nanoshell using MCS parameter can be expressed as [120]:

$$\delta T = \int_Z \iint_A \rho \left\{ \begin{array}{l} \left(\frac{\partial u}{\partial t} + z\frac{\partial \psi_x}{\partial t}\right)\left(\frac{\partial}{\partial t}\delta u + z\frac{\partial}{\partial t}\delta\psi_x\right) \\ + \left(\frac{\partial v}{\partial t} + z\frac{\partial \psi_\theta}{\partial t}\right)\left(\frac{\partial}{\partial t}\delta v + z\frac{\partial}{\partial t}\delta\psi_\theta\right) + \left(\frac{\partial w}{\partial t}\right)\frac{\partial}{\partial t}\delta w \end{array} \right\} R\,dz\,dx\,d\theta$$

$$(18)$$

For the composite layer reinforced with uniform (UD) of FG distribution of GPLs, Fourier heat conduction relation can be formulated as:

$$\frac{1}{z} k_z \frac{\partial}{\partial z}\left(z\frac{\partial T}{\partial z}\right) + k_x \frac{\partial^2 T}{\partial x^2} = 0 \qquad \text{for } UD$$

$$\frac{1}{z} \frac{\partial}{\partial z}\left(k_z z\frac{\partial T}{\partial z}\right) + k_x \frac{\partial^2 T}{\partial x^2} = 0 \qquad \text{for } FG$$

$$(19)$$

In addition, thermal surface boundary conditions are as follows:

$$T(x, \theta, -h/2) = T_i, \ \ T(x, \theta, h/2) = T_0, \ \ T(0, \theta, z) = T(L, \theta, z) = 0$$

$$(20)$$

The work done by applied forces can be written as:

$$W_2 = \frac{1}{2}\left\{q_{\text{dynamic}} w^2\right\} R\,dV$$

$$(21)$$

In which q_{dynamic} is the transverse force due to applied dynamic load. Substituting Eqs. (10), (16), (17) into Eq. (9) and integrating by part, the equations of motion and boundary conditions of the GNP cylindrical nanoshell in thermal environment using MCS parameter can be obtained as follows:

$$\left[\frac{\partial N_{xx}}{\partial x} + \frac{1}{R}\frac{\partial N_{x\theta}}{\partial \theta} + \frac{1}{2R^2}\left(-\frac{\partial Y_{\theta\theta}}{\partial \theta} + \frac{\partial Y_{zz}}{\partial \theta}\right) + \frac{1}{2R}\frac{\partial^2 Y_{zx}}{\partial \theta\,\partial x} + \frac{1}{2R^2}\frac{\partial^2 Y_{\theta z}}{\partial \theta^2}\right]\delta u$$

$$+\left[\frac{\partial N_{x\theta}}{\partial x} + \frac{1}{R}\frac{\partial}{\partial \theta}N_{\theta\theta} + \frac{Q_{z\theta}}{R} + \frac{1}{2}\left\{\frac{1}{R}\frac{\partial}{\partial x}(-Y_{xx} + Y_{\theta\theta}) - \frac{1}{R^2}\frac{\partial Y_{\theta x}}{\partial \theta} - \frac{\partial^2 Y_{xz}}{\partial x^2} - \frac{Y_{xz}}{R^2} - \frac{1}{R}\frac{\partial^2 Y_{z\theta}}{\partial \theta\,\partial x}\right\}\right]\delta v$$

$$-N_2^T\frac{\partial^2 v}{\partial x^2}\delta v + \left[\frac{\partial Q_{xz}}{\partial x} + \frac{1}{R}\frac{\partial Q_{z\theta}}{\partial \theta} - \frac{N_{\theta\theta}}{R} - \frac{1}{2R^2}\frac{\partial^2 Y_{\theta x}}{\partial \theta^2} - \frac{1}{2R^2}\frac{\partial Y_{zx}}{\partial \theta} + \frac{1}{2R}\frac{\partial Y_{\theta z}}{\partial x} + \frac{\partial^2 Y_{x\theta}}{2\partial x^2}\right]\delta w_0$$

$$+\left[-\frac{1}{2R}\frac{\partial^2}{\partial \theta\,\partial x}(Y_{xx} - Y_{\theta\theta}) - N_1^T\frac{\partial^2 w}{\partial x^2}\right]\delta w_0 + \left[\frac{\partial M_{xx}}{\partial x} + \frac{1}{R}\frac{\partial M_{\theta\theta}}{\partial \theta} - Q_{xz} + \frac{1}{2}\frac{\partial Y_{\theta x}}{\partial x} - \frac{1}{2R}\frac{\partial}{\partial \theta}(Y_{zz} - Y_{\theta\theta})\right]\delta\psi_x$$

$$+\left[\frac{Y_{zz}}{R} + \frac{1}{2R}\frac{\partial^2 T_{zx}}{\partial \theta\,\partial x} + \frac{1}{2R^2}\frac{\partial^2 T_{\theta z}}{\partial \theta^2}\right]\delta\psi_x + \left[\frac{1}{R}\frac{\partial M_{\theta\theta}}{\partial \theta} + \frac{\partial M_{x\theta}}{\partial x} - Q_{z\theta} + \frac{1}{2}\frac{\partial}{\partial x}\left(Y_{zz} - Y_{xx} + \frac{T_{\theta\theta}}{R}\right)\right]\delta\psi_\theta$$

$$+\left[-\frac{1}{2}\frac{\partial Y_{\theta x}}{\partial \theta} + \frac{Y_{xz}}{2R} - \frac{1}{2R}\frac{\partial^2 T_{\theta z}}{\partial \theta\,\partial x} - \frac{1}{2}\frac{\partial^2 T_{zx}}{\partial x^2}\right]\delta\psi_\theta = \left\{I_0\frac{\partial^2 u}{\partial t^2} + I_1\frac{\partial^2 \psi_x}{\partial t^2}\right\}\delta u + \left\{I_0\frac{\partial^2 v}{\partial t^2} + I_1\frac{\partial^2 \psi_\theta}{\partial t^2}\right\}\delta v$$

$$+I_0\frac{\partial^2 w}{\partial t^2}\delta w_0 + \left\{I_1\frac{\partial^2 u}{\partial t^2} + I_2\frac{\partial^2 \psi_x}{\partial t^2}\right\}\delta\psi_x + \left\{I_1\frac{\partial^2 v}{\partial t^2} + I_2\frac{\partial^2 \psi_\theta}{\partial t^2}\right\}\delta\psi_\theta + q_{\text{dynamic}}\delta w$$

$$(22)$$

In addition, governing equations and boundary conditions are given in Appendix A.

4 Solution procedure

In this section, analytical method is implemented to solve the governing equations of MSGT-based on GPLRC nanoshell. In addition, in this research, the proposed model is simply supported in $x = 0, L$ and $\theta = \pi/2, 3\pi/2$. Thus, the displacement fields can be calculated as:

$$
\begin{Bmatrix}
u_0(x, \theta, t) \\
v_0(x, \theta, t) \\
w_0(x, \theta, t) \\
\psi_x(x, \theta, t) \\
\psi_\theta(x, \theta, t)
\end{Bmatrix}
= \sum_{m=1}^{\infty} \sum_{n=1}^{\infty}
\begin{Bmatrix}
U_{0mn} \cos\left(\frac{m\pi}{L}x\right) \cos(n\theta) \\
V_{0mn} \sin\left(\frac{m\pi}{L}x\right) \sin(n\theta) \\
W_{0mn} \sin\left(\frac{m\pi}{L}x\right) \cos(n\theta) \\
\psi_{xmn} \cos\left(\frac{m\pi}{L}x\right) \cos(n\theta) \\
\psi_{\theta mn} \sin\left(\frac{m\pi}{L}x\right) \sin(n\theta)
\end{Bmatrix}
\sin(\omega t)
$$

(23)

where $\{U_{0mn}, V_{0mn}, W_{0mn}, \Psi_{xmn}, \Psi_{\theta mn}\}$ are the unknown Fourier coefficients that need to be determined for each n and m values. Also, n and m are the circumferential and axial wave numbers, respectively. For vibration analysis of the structure, by substituting Eq. (21) into governing equations, one obtains [121–126]:

$$
\left(
\begin{Bmatrix}
K_{11} & K_{12} & K_{13} & K_{14} & K_{15} \\
K_{21} & K_{22} & K_{23} & K_{24} & K_{25} \\
K_{31} & K_{32} & K_{33} & K_{34} & K_{35} \\
K_{41} & K_{42} & K_{43} & K_{44} & K_{45} \\
K_{51} & K_{52} & K_{53} & K_{54} & K_{55}
\end{Bmatrix}
- \omega_{ex}^2
\begin{Bmatrix}
M_{11} & M_{12} & M_{13} & M_{14} & M_{15} \\
M_{21} & M_{22} & M_{23} & M_{24} & M_{25} \\
M_{31} & M_{32} & M_{33} & M_{34} & M_{35} \\
M_{41} & M_{42} & M_{43} & M_{44} & M_{45} \\
M_{51} & M_{52} & M_{53} & M_{54} & M_{55}
\end{Bmatrix}
\right)
$$

$$
\begin{pmatrix}
U_0 \\
V_0 \\
W_0 \\
\psi_x \\
\psi_\theta
\end{pmatrix}
=
\begin{bmatrix}
0 \\
0 \\
q_{\text{dynamic}} \\
0 \\
0
\end{bmatrix}
\begin{bmatrix}
U_0 \\
V_0 \\
W_0 \\
\psi_x \\
\psi_\theta
\end{bmatrix}
$$

(24)

It should be noted that stiffness and mass components are given in Appendix A. In Eq. (22), ω_{ex} is the excitation frequency and applied dynamic load (q_{dynamic}) is defined as:

$$
q_{dynamic} = \sum_{m=1}^{\infty} \sum_{n=1}^{\infty} q_0 \sin\left(\frac{m\pi}{L}x\right) \cos(n\theta) \sin(\omega t),
$$

(25)

Solution of Eq. (23) gives the dynamic deflection and excitation frequency of the porous FG-GPLRC cylindrical nanoshell. The dimensionless excitation frequency and forced vibration amplitude are defined as:

$$
\Omega = 10 \times \omega_{ex} L \sqrt{\rho/E}, \qquad \overline{W}_{\text{uniform}} = W_{0mn} \frac{10Eh^3}{L^4 q_0}
$$

(26)

5 Temperature field

To satisfy temperature boundary conditions, Eq. (18), following Fourier series solution to Eqs. (30), (31) is assumed

$$
T = \sum_{m=1}^{\infty} \sin\left(P_m x\right) \cos(n\theta)
$$

(27)

where $P_m = \frac{m\pi}{L}$. Thermal conductivity coefficients regarding to each GPLs distribution pattern can be determined as

$$
\frac{k_i}{k_m} = 1 + D_i \quad \text{for UD}
$$

(28)

$$
\frac{k_i}{k_m} = 1 + 2D_i\left(\frac{z - r_i}{h}\right) \quad \text{for FG} - \text{A}
$$

(29)

$$
\frac{k_i}{k_m} = 1 + 2D_i\left|1 - \frac{2(z - r_i)}{h}\right| \quad \text{for FG} - \text{X}
$$

(30)

$$
\frac{k_i}{k_m} = 1 + 2D_i\left(\frac{z - r_i}{\frac{h}{2}}\right) \quad \text{for } z \le r_i + \frac{h}{2} \quad \text{for FG} - \text{O}
$$

$$
\frac{k_i}{k_m} = 1 + 2D_i\left(\frac{r_o - h_p - z}{\frac{h}{2}}\right) \quad \text{for} \quad z \ge r_i + \frac{h}{2} \quad \text{for} \quad \text{FG} - \text{O}
$$

(31)

where $D_i = \frac{P_3 V_{GPL}}{3} \times \frac{\frac{k_{iGPL}}{k_m}}{P_3 + \left(\frac{2a_k}{d} \times \frac{k_{iGPL}}{k_m}\right)}; (i = z, x); a_k = R_k k_m$.

Temperature gradient of radial coordinate for UD pattern of GPLs can be obtained by implementing Eqs. (25) and (26) in Eq. (17) as follows

$$
T_m(z) = B_1 I_o(qz) + C_1 K_o(qz)
$$

(32)

where $q = P_m \sqrt{\frac{k_x}{k_z}}$ and B_1, C_1 are constants of integration which can be obtained from thermal surface boundary conditions at the inner and outer surfaces of layer reinforced with UD pattern of GPLs (More information is presented in Appendix B). From Eqs. (25), (27, 28, 29), heat conduction differential equation, Eq. (17) would be reduced to Heun's differential equation as following

$$
\left(A_1 z^2 + A_2 z^3\right)\frac{\partial^2 T}{\partial z^2} + \left(2A_2 z^2 + A_1 z\right)\frac{\partial T}{\partial z} + \left(A_3 z^2 + A_4 z^3\right)T = 0
$$

(33)

Here A_1, A_2,..., A_6 are constant coefficients depending on the pattern of GPLs distribution (see Appendix B). Analytical solution is determined for Eq. (31) according to subsequent relation

$$T(z) = HeunC\left(\frac{2A_1}{A_2}\sqrt{-\frac{A_4}{A_2}}, 0, 0, \frac{A_1}{A_2^3}(A_1A_4 - A_2A_3), 0, -\frac{A_2}{A_1}r\right)e^{-\sqrt{-\frac{A_4}{A_2}}} \times$$

$$\left\{B_2 \int_{r_i}^{r_o} \frac{e^{2\sqrt{-\frac{A_4}{A_2}}z}}{z(A_2z + A_1)\left(HeunC\left(\frac{2A_1}{A_2}\sqrt{-\frac{A_4}{A_2}}, 0, 0, \frac{A_1}{A_2^3}(A_1A_4 - A_2A_3), 0, -\frac{A_2}{A_1}z\right)\right)^2}dz + C_2\right\} \quad (34)$$

where B_2 and C_2 are constant coefficients of integration which would be computed from thermal surface boundary conditions applied at the inner and outer surface of the layer reinforced with FG distribution patterns of GPLs (see Appendix B). By employing Eq. (25) and (32) leads to the following heat conduction equation in the form of modified Bessel differential equation

$$z^2\frac{\partial^2 T_a}{\partial z^2} + z\frac{\partial T_a}{\partial z} - (m_a^2z^2)T_a = 0 \quad (35)$$

Here $m_a = p_m\sqrt{\frac{k_{ax}}{k_{az}}}$. Solution to Eq. (33) for the actuator layers are as

$$T_a(z) = B_3I_o(m_az) + C_3K_o(m_az) \quad (36)$$

where I_o, K_o are modified Bessel function of the first kind and second kind of zero order, respectively; B_3, C_3 are constant of integration which are determined from surface temperature boundary condition (Appendix B).

6 Results and discussion

In the result section, the GNP cylindrical nanoshell in a thermal environment under various thermal loading is modeled for the simply supported boundary conditions. After the modeling of the current structure using FMCS parameter, the effects of GNP distribution pattern, modified couple stress parameter, length to radius ratio, mode number, and thermal environment on resonance frequency and dynamic deflection are studied. In the next section will be shown that, these elements have important role on the dynamic behavior of the presented structure. However, results section of our paper are divided into two sections. In the first section, validation of our model with the aid of previous papers of the literature is presented. In the second section, effects of various thermal loading and some various parameters on the resonance frequency, thermal buckling and dynamic deflection of a GNP nanoshell in thermal environments are presented.

6.1 Model validation

Table 1 illustrates a comparison study between the results of this paper and literatures of the simply supported nanoshell with considering modified couple stress theory. Beni et al. [127] investigated vibrational analysis of the FG cylindrical thin nanoshell using modified couple stress theory. It can be seen there is good agreement between the dimensionless natural frequency of the current study and the results of Ref. [127]. As another verification for this work, according to Fig. 4, it is revealed that the suggested modeling can provide good agreement with MD simulation. Figure 4 shows that, as $l = R/3$, the results of the current research are very similar to those of MD simulation. The material properties of SWNT are presented in Table 2.

6.2 Parametric results

In this section, analytical results are indicated for simply supported a GNP cylindrical nanoshell in thermal environments under various thermal loadings. In the present paper, the GNP nanostructure with a total thickness $h_{GNP} = 1.5$ nm, length of $a_{GNP} = 2.5$ mμ and Radius of $R_{GNP} = 0.75$ mμ. Table 3 is included mechanical properties of GNP. Now, in this section, the effects of different parameters on the excitation frequency, dimensionless amplitude and relative frequency changes of the structure are investigated.

Temperature dependent of the GNP materials is shown as follow [129]:

$\alpha_m = 45(1 + 0.0005\Delta T) \times 10^{-6}/K$ and $E = (3.52 - 0.0034T)$ GPa, in which $T = T_0 + \Delta T$.

Figure 5 shows thermal buckling mode shape of GNP CNTRC cylindrical nanoshell versus the dimensionless

cylindrical shell length. To have a better view of the mode shapes, the vertical displacement of the nanoshell is normalized according to the maximum displacement of the thermal buckling mode shape.

6.3 The effect of different parameters on relative frequency change

The percentage value in parentheses denotes the relative frequency increase ($\omega_C - \omega_M$), where ω_C and ω_M are natural frequencies with and without GPL, respectively. Figure 6 shows the relative frequency changes of the FG-GPLRC cylindrical nanoshell with different total number of layers (N_L). As expected, the fundamental frequencies of the structure with GPL distribution pattern 1 are not affected by N_L since they are homogeneous. For the cylindrical nanoshells with pattern 2 in which GPLs are non-uniformly dispersed, their fundamental frequencies decrease with increasing the total number of layers to $N_L = 7$, then they remain almost unchanged when N_L is further increased. In contrast, this trend is reversed for GPL distribution pattern 3. Among the three non-uniform patterns considered, the fundamental frequency of the structure with GPL patterns 1 and 4 is least affected by the change in N_L. According to this figure by increasing the number of layers ($1 < N_L < 7$) the natural frequency and stability of the nanostructure change (for non-uniform GPL distribution patterns 2 and 3). It is observed that, in the non-uniform GPL distribution pattern 3, by increasing of the number of layers, the natural frequency and stability of the nanostructure increase. Also, for the other uniform and non-uniform distribution patterns, number of layers of the GPL is not important. The other amazing result is that, by increasing the number of layers in the non-uniform GPL distribution pattern 2, the natural frequency and stability decrease.

Figure 7 shows the effects of mode number and weight function on the relative frequency change of the GNP cylindrical nanoshell. Based on Fig. 7, an increase in the mode number causes to improve in the relative frequency and decreases the stability of the structure. The amazing results is that; weight function has direct effect on relative frequency change of the GNP cylindrical nanoshell. This is because, by increasing the weight function, the structure become softer and it is a reason for increasing the relative frequency change.

In Table 4, the effects of different GNP distribution pattern, FMCS parameter, and thermal distribution on natural frequency of the GNP-nanosturacture are shown. It can be seen from the table that as GNP distribution pattern increases from 1 to 4, the behavior of the natural frequency depends on the type of pattern. For example, the patterns 2 and 3 of the GNP have the higher and lower natural frequency. For better comprehensive, the GPL with pattern 2

Table 1 Comparison of dimensionless first three natural frequencies of isotropic homogeneous nanoshells, with different thicknesses, $L/R = 10$ and $m = 1$

h/R	n	Ref. [127] ($l=0$)	Present ($l=0$)	Ref. [127] ($l=h$)	Present study ($l=h$)
0.02	1	0.1954	0.19536215	0.1955	0.19543206
	2	0.2532	0.25271274	0.2575	0.25731258
	3	0.2772	0.27580092	0.3067	0.30621690
0.05	1	0.1959	0.19542305	0.1963	0.19585782
	2	0.2623	0.25884786	0.2869	0.28543902
	3	0.3220	0.31407326	0.4586	0.45457555

has higher stability in comparison with other patterns. It is observed that by increasing the FMCS parameter to radius ratio (l/R), the natural frequency increases. Also, the results show that the nonlinear temperature change (NLT) has higher effect on natural frequency in comparison with the linear temperature change (LT).

Figures 8 and 9 show the effects of MCS and classic theories on the relative frequency changes of the GNP cylindrical nanoshell, respectively. According to these figures, an increase in the temperature change causes to improve in the relative frequency and decrease the stability of the structure. Relative frequency increases smoothly when the temperature change increases. At a certain value of temperature change, a notable increase in relative frequency of the structure is observed. The reason of this phenomena is that, the buckling at this temperature occurs. The amazing results is that, MCS theory has higher effect on critical temperature of the structure in comparison with classic theory. So, for modelling of the nanostructures should be attention to the size-dependent theories specially MCS theory. Also, weight function has direct effect on relative frequency changes of the GNP cylindrical nanoshell. This is because, by increasing the weight function, the structure become softer and it is a reason for increasing the relative frequency change.

6.4 The effects of different parameter on excitation frequency and dimensionless amplitude

In Fig. 10, the effect of weight function on dynamic deflection and resonance frequency was presented for the GNP/nanostructure. Also, in this figure, different values' function (g_{GNP}) effects are examined. It is evident that, dynamic deflection of the GNP cylindrical nanoshell is affiliated by the value of excitation frequency of dynamic load. By increasing the excitation frequency can see smoothly increase for dynamic deflection. At a specific value of excitation frequency, a remarkable increase in deflection of GNP cylindrical nanoshell is observed. The reason is that the resonance phenomena occurs if the dynamic deflection tends to infinity. With decreasing the weight function, it is observed that, resonance frequency of the GNP cylindrical nanoshell
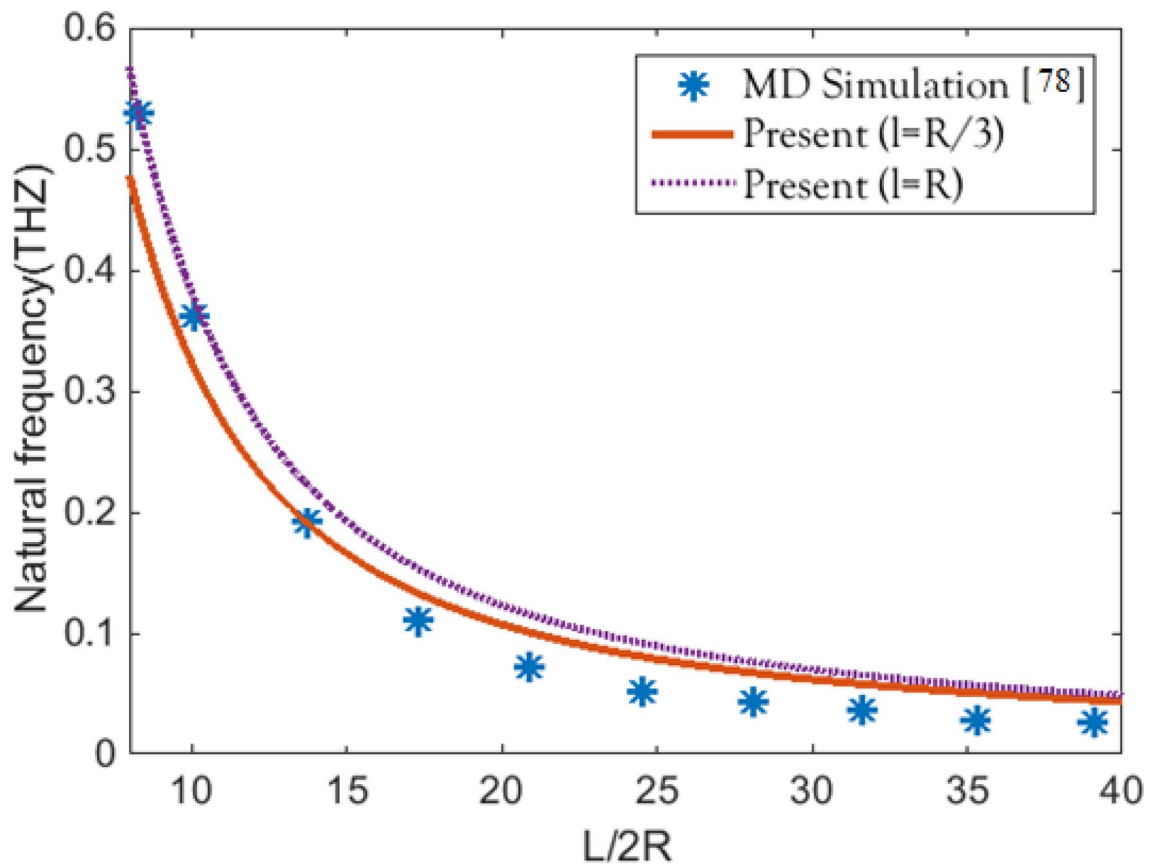
Fig. 4 Comparison of the natural frequency of cylindrical nanoshell with the results obtained by MD simulation [128]

Table 2 The material properties of single-walled carbon nanotube

E	vv	H	$\rho\rho$
1.06 TPa	0.19	0.34 nm	2300 kg/m^3

Table 3 Material properties of the epoxy and GNP [129]

Material properties:	Epoxy	GNP
Young's modulus (GPa)	3	1010
Density (kg m^{-3})	1200	1062.5
Poisson's ratio	0.34	0.186
Thermal expansion coefficient(10^{-6}/K)	60	5

decreases. The reason for this issue is that, stiffness, resonance frequency and stability of a structure improved due to increasing weight function.

In Fig. 11, the effect of different GNP distribution pattern on dynamic deflection and resonance frequency of the GNP nanosturacture is shown. It can be seen from the graph that as GNP distribution pattern increases from 1 to 4, the resonance frequency increases, this leads to an increase in

the instability of structure. In other words, A-GNPRC gives larger resonance frequency than other patterns. Also, the resonance frequency of the structure, in the pattern 4 is more similar to pattern 3. The reason of this issue is in the mathematical function which is presented in previous section.

In Fig. 12, the effects of FMCS parameter on forced vibration of GNP cylindrical nanoshell for X-GNPRC pattern are presented. As an important result, can see that the FMCS parameter has significantly effect on the resonance frequency of the structure. It can be seen from the diagram, by improving the FMCS parameter the resonance frequency of the structure increases. Also, this phenomenon improves the stability of the GNP cylindrical nanoshell. It should be mentioned that, as the FMCS parameter is equal to zero, the classic theory occurs.

For investigation of radius-to-thickness ratio (R/h) and temperature change effects on resonance frequency of the GNP cylindrical nanoshell Figs. 13 and 14 is drawn, respectively. According to Fig. 13, it can be observed that by increasing the R/h ratio, the resonance frequency and stability decline. As it mentioned earlier, by increasing the temperature difference, the stability and resonance frequency decrease.

Fig. 5 The thermal buckling mode shapes of the cylindrical microshell in this study
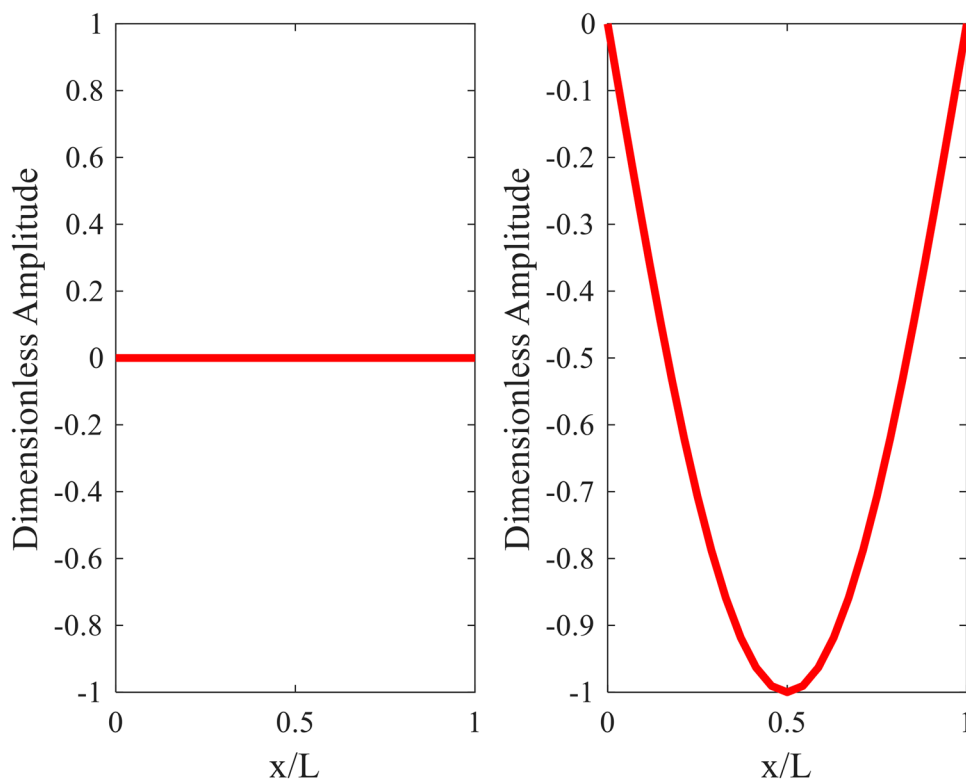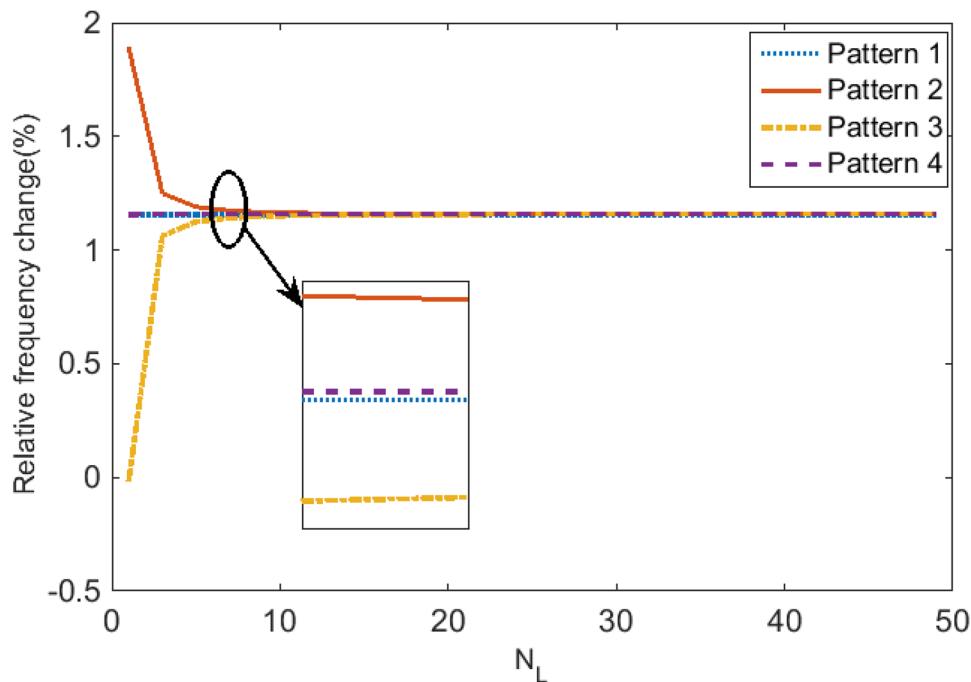

Fig. 6 Effect of total number of layers NL on the percentage fundamental frequency change for different patterns of GNP/epoxy ($\Delta T = 10K$, $l = R/3$, Pattern2, $L/R = 10$, $R/h = 10$ and $n = m = 1$)


7 Conclusion

This article presents the size-dependent free and forced vibration characteristics of a composite cylindrical nanoshell reinforced with GNP under bi-directional thermal loading.

The size-dependent GNP nanoshell is analyzed using FMCS parameter. The equations of motion and non-classic boundary conditions are derived using the Hamilton's principle. Also, the results of current model were validated with those obtained by molecular dynamics (MD) simulation. The

Fig. 7 Effect of weight function on the percentage fundamental frequency change for different mode numbers ($\Delta T = 10K$, $l = R/3$, Pattern2, $L/R = 10$, $R/h = 10$)
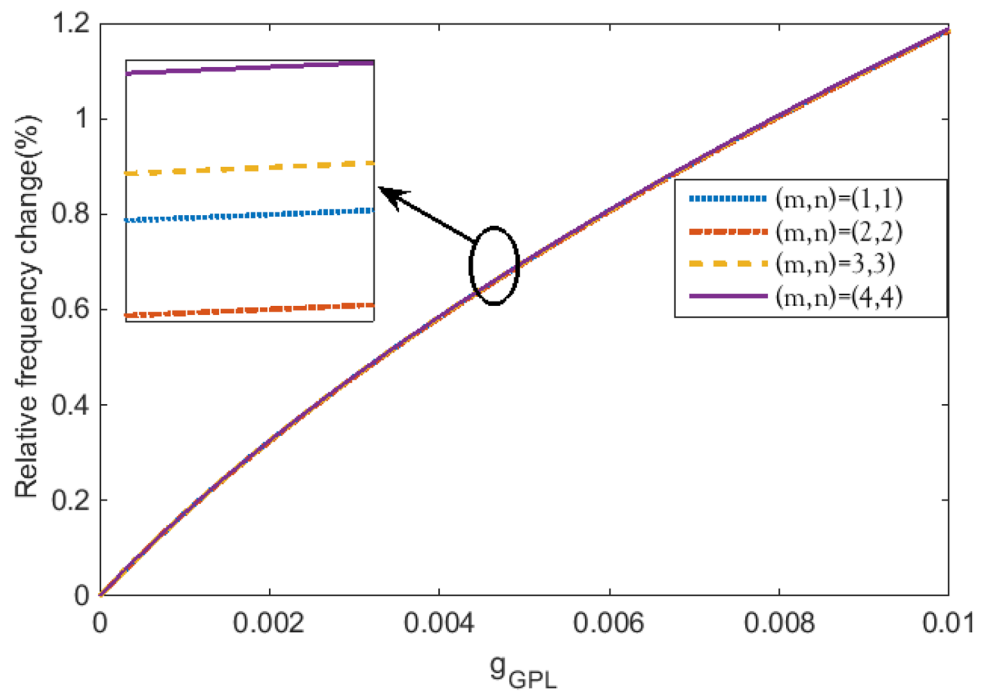
influence of some key parameters such as, various thermal loading, GNP distribution pattern, modified couple stress parameter, length to radius ratio, mode number and thermal environment on the resonance frequency, relative frequency change and dynamic deflection of the GNP nanoshell were studied. In this study, the following main results can be achieved:

(1) The results show that the nonlinear temperature changes (NLT) have higher effect on the natural frequency in comparison with the linear temperature changes (LT).1) The results show that the nonlinear temperature changes (NLT) have higher effect on the natural frequency in comparison with the linear temperature changes (LT).

(2) It was observed that the resonance frequency is increased when the modified couple stress parameter and weight function increase and decreased when the temperature difference increases.

(3) The results show that A-GNP gives larger resonance frequency than other patterns.

(4) The results show that an increase in the temperature change causes an increase in the relative frequency change and decrease the stability of the structure.

(5) With an increase in the radius-to-thickness ratio the resonance frequency and stability of the GNP cylindrical nanoshell tends to increase.

Appendix A

The components of the matrices in Eq. (24):

$$K_{11} = \left\{ \begin{array}{l} A_{11}(-m^2) - A_{66}\left(\dfrac{n}{R}\right)^2 + \dfrac{A_{77}l^2n^2}{4R^2}(-m^2) \\ + \left(-\dfrac{A_{77}l^2n^4}{4R^4}\right) - \dfrac{A_{77}l^2n^2}{R^4} \end{array} \right\}$$

$$K_{12} = \left\{ \begin{array}{l} \dfrac{A_{12}n}{R}(m) + \dfrac{A_{66}n}{R}(m) + \dfrac{A_{77}l^2n}{4R}(-m^3) \\ + \left(\dfrac{A_{77}l^2(-n-n^3)}{4R^3}\right)(m) \end{array} \right\}$$

$$K_{13} = \left\{ \dfrac{A_{12}}{R}(m) - \left(\dfrac{A_{77}l^2n^2}{2R^3}\right)(m) \right\}$$

$$K_{14} = \left\{ \begin{array}{l} B_{11}(-m^2) - B_{66}\dfrac{n^2}{R^2} + \dfrac{B_{77}l^2n^2}{4R^2}(-m^2) \\ + \left(\dfrac{5A_{77}l^2n^2}{4R^3} - \dfrac{B_{77}l^2n^4}{4R^4}\right) \end{array} \right\}$$

Table 4 The effects of different FMCS parameter to radius ratio, pattern of GNP and temperature on natural frequency (GHz) of the GNPRC nanoshell with $L/R = 10$, $R/h = 10$, $g_{GPL} = 1\%$ and different thermal distributions

		$\Delta T = 20$		$\Delta T = 40$		$\Delta T = 60$	
		LT	NLT	LT	NLT	LT	NLT
Pattern 1	l/R						
	0	1.948752	1.982586	1.904938	1.973578	1.859902	1.964363
	1/3	2.070645	2.102498	2.028391	2.092946	1.985038	2.083173
	1/2	2.184729	2.214933	2.143707	2.204870	2.101676	2.194574
	2/3	2.302991	2.331662	2.263052	2.321068	2.222178	2.310231
Pattern 2	l/R						
	0	1.947517	1.981282	1.903786	1.972283	1.858836	1.963078
	1/3	2.069517	2.101302	2.027344	2.091759	1.984077	2.081997
	½	2.183646	2.213784	2.142704	2.203735	2.100757	2.193447
	2/3	2.301909	2.330516	2.262047	2.319933	2.221255	2.309107
Pattern 3	l/R						
	0	1.951057	1.984761	1.907392	1.975764	1.862513	1.966560
	1/3	2.072872	2.104606	2.030755	2.095065	1.987547	2.085304
	1/2	1.186938	2.217031	2.146045	2.206980	2.104149	2.196697
	2/3	2.305233	2.333800	2.265415	2.323218	2.224670	2.312393
Pattern 4	l/R						
	0	1.949577	1.983336	1.905848	1.974335	1.860901	1.965126
	1/3	2.073030	2.104788	2.030885	2.095243	1.987647	2.085479
	1/2	2.188392	2.218488	2.147493	2.208434	2.105592	2.198148
	2/3	2.307948	2.336501	2.268143	2.325918	2.227411	2.315091

Fig. 8 The effects of temperature change and classical theory on the relative frequency change for different weight function and linear temperature change (LT) (Pattern4, $L/R = 10$, $R/h = 10$ and $n = m = 1$)
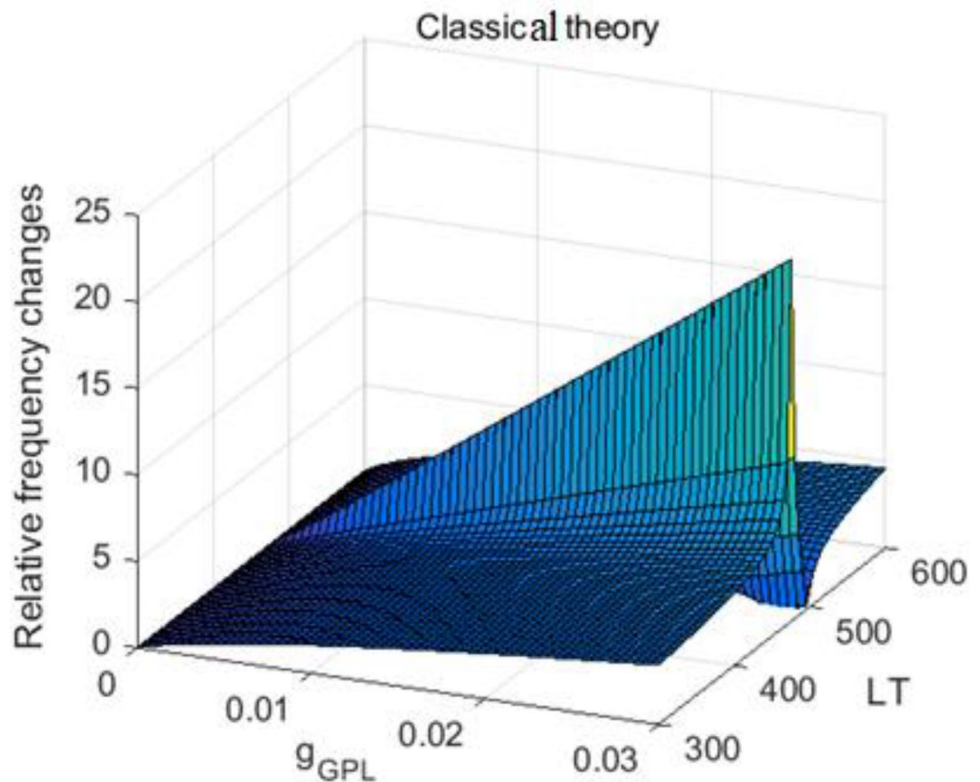
Fig. 9 The effects of temperature change and MCS theory on the relative frequency change for different weight function and linear temperature change (LT) (Pattern4, $L/R = 10$, $R/h = 10$ and $n = m = 1$)
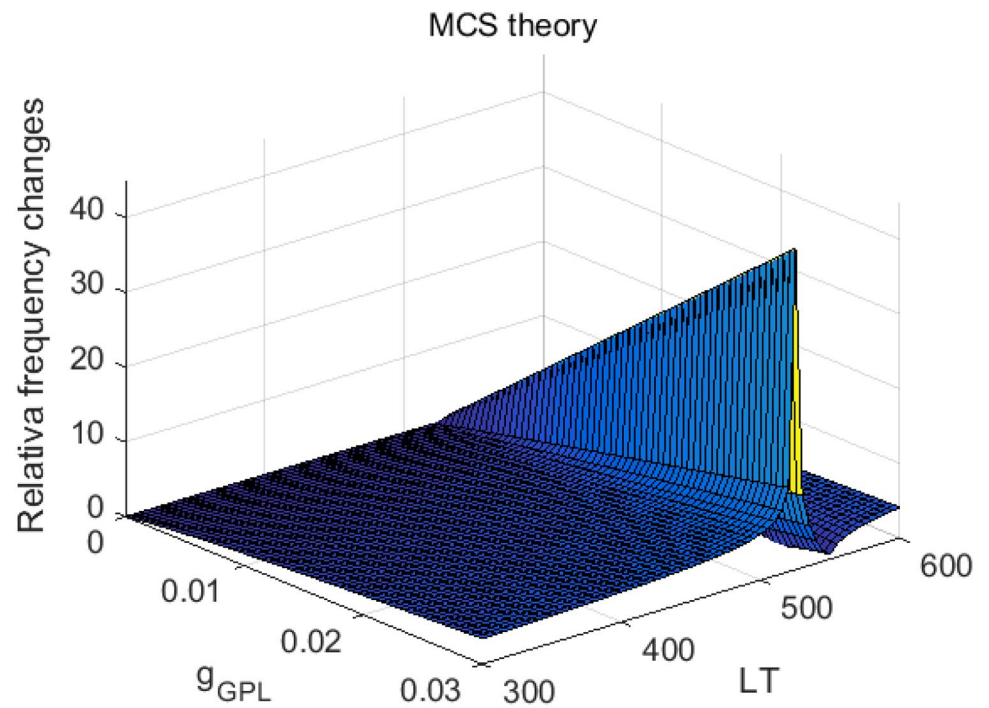

Fig. 10 Dynamic deflection and resonance frequency of the cylindrical nanoshell for different weight function ($\Delta T = 20K$, $l = R/3$, Pattern2, $L/R = 10$, $R/h = 10$ and $n = m = 1$)
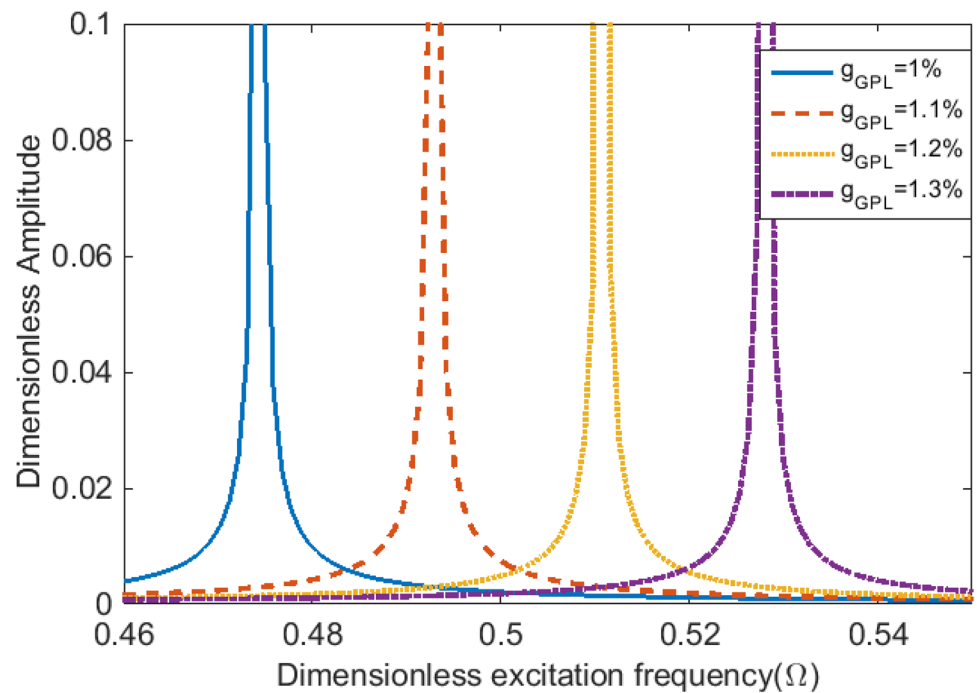
Fig. 11 Dynamic deflection and resonance frequency of the cylindrical nanoshell for different GNP distribution patterns ($\Delta T = 20K$, $l = R/3$, $L/R = 10$, $R/h = 10$ and $n = m = 1$)
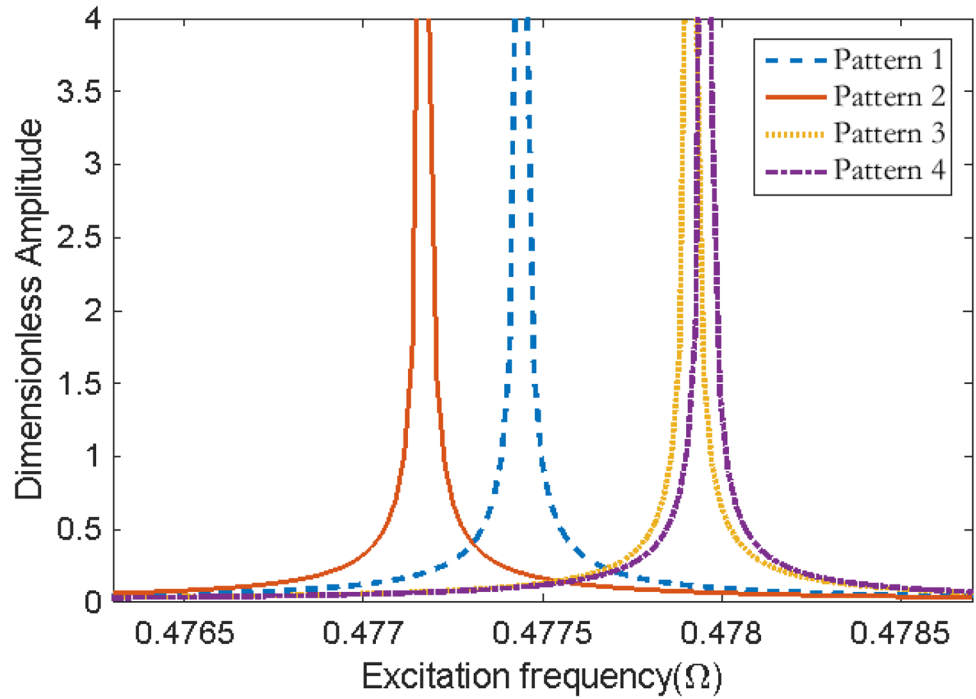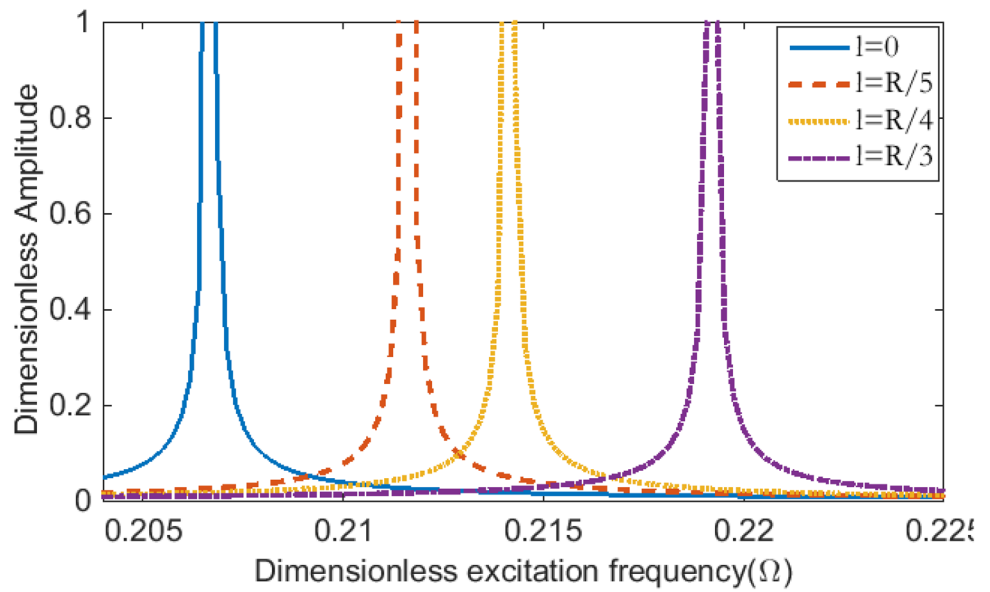

Fig. 12 Dynamic deflection and resonance frequency of the cylindrical nanoshell for different modified couple stress parameter ($\Delta T = 20K$, Pattern2, $L/R = 10$, $R/h = 10$ and $n = m = 1$)

$$K_{15} = \left\{ \begin{array}{l} \dfrac{B_{12}n}{R}(m) + \dfrac{B_{66}n}{R}(m) + \dfrac{B_{77}l^2n}{4R}(-m^3) \\ -\left(\dfrac{(B_{77})l^2n}{2R^3} + \dfrac{A_{77}l^2n}{4R^2} - \dfrac{B_{77}l^2n^3}{4R^3} \right)(m) \end{array} \right\}$$

$$K_{21} = -\left\{ \begin{array}{l} +\dfrac{A_{12}n}{R}(-m) + \dfrac{A_{66}n}{R}(-m) + \dfrac{A_{77}l^2n}{4R}(m^3) \\ +\left(\dfrac{A_{77}l^2(-n-n^3)}{4R^3} \right)(-m) \end{array} \right\}$$

Fig. 13 Dynamic deflection and resonance frequencies of the cylindrical nanoshell for different radius to thickness ratios ($\Delta T = 0K$, $l = R/3$, Pattern4, $L/R = 10$ and $n = m = 1$)
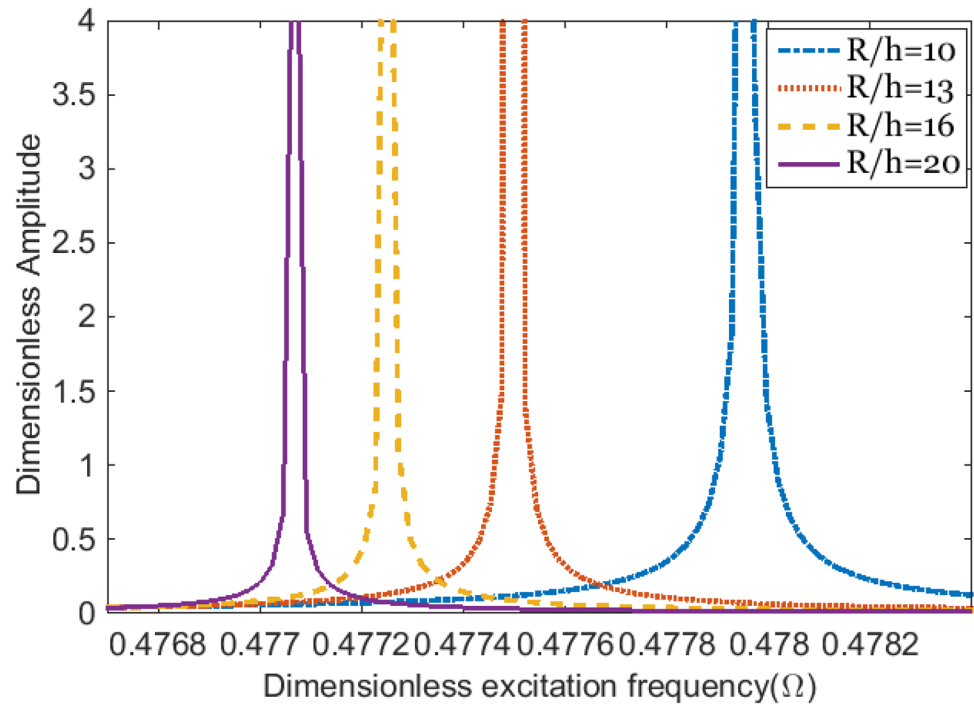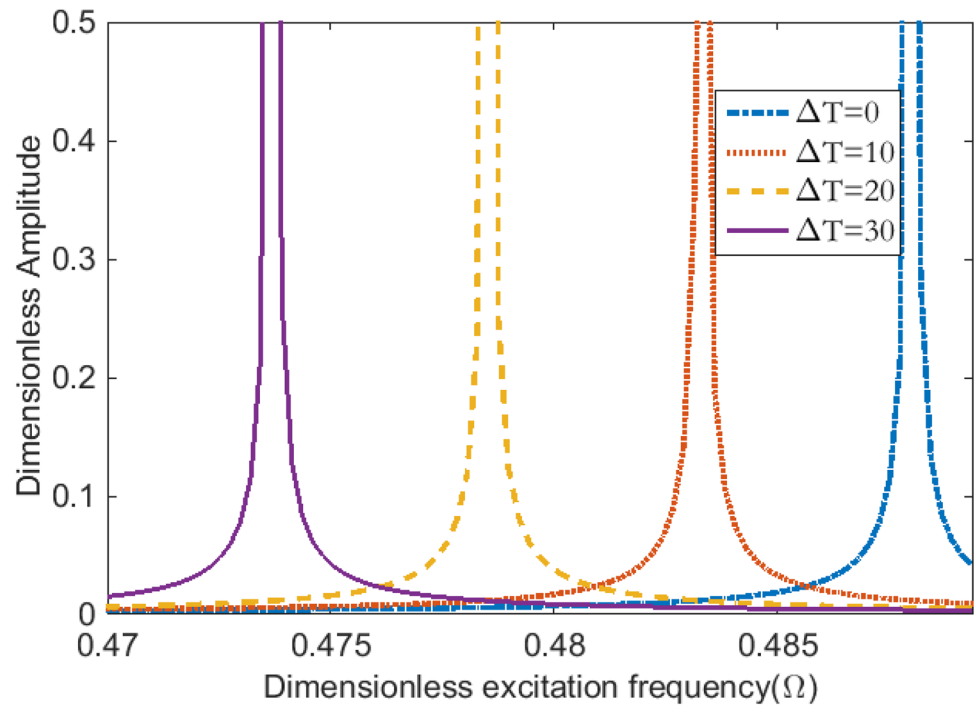

Fig. 14 Dynamic deflection and resonance frequencies of the cylindrical nanoshell for different temperature changes ($l = R/3$, Pattern4, $L/R = 10$, $R/h = 10$ and $n = m = 1$)

$$K_{22} = \left\{ \begin{array}{l} A_{66} \sum_{k=1}^{i} (-m^2) - A_{11}\left(\dfrac{n}{R}\right)^2 - \dfrac{k_s A_{66}}{R^2} - \dfrac{A_{77}l^2}{4}(m^4) \\[2mm] + \left(\dfrac{A_{77}l^2(2+n^2)}{4R^2}\right)(-m^2) \\[2mm] + \left(-\dfrac{A_{77}l^2(1+n^2)}{4R^4}\right) - N_h\dfrac{n}{R^2} \end{array} \right\}$$

$$K_{23} = \left\{ \begin{array}{l} -A_{11}\dfrac{n}{R^2} - k_s A_{66}\dfrac{n}{R^2} + \left(\dfrac{A_{66}l^2 n}{4R^2}\right)(-m^2) \\[2mm] + \left(-\dfrac{A_{566}l^2(n^3+n)}{4R^4}\right) \end{array} \right\}$$

$$K_{24} = \left\{ \begin{array}{l} -\dfrac{B_{66}n}{R}(-m) - \dfrac{B_{12}n}{R}(-m) - \dfrac{B_{77}l^2 n}{4R}(m^3) \\[2mm] - \left(\dfrac{A_{77}l^2 n}{2R^2} + \dfrac{B_{77}l^2(-n^3+n)}{4R^3}\right)(-m) \end{array} \right\}$$

$$K_{25} = \left\{ \begin{array}{l} B_{66}(-m^2) - B_{11}\left(\dfrac{n}{R}\right)^2 + \dfrac{k_s A_{55}}{R} - \dfrac{B_{77}l^2}{4}(m^4) \\[2mm] - \left(\dfrac{-3A_{77}l^2}{4R} - \dfrac{B_{77}l^2}{2R} - \dfrac{B_{77}l^2(n^2-1)}{4R^2}\right)(-m^2) \\[2mm] + \left(\dfrac{A_{77}l^2(1-n^2)}{4R^3}\right) \end{array} \right\}$$

$$K_{31} = -\left\{ +\dfrac{A_{12}}{R}(-m) - \left(\dfrac{A_{77}l^2 n^2}{2R^3}\right)(-m) \right\}$$

$$K_{32} = \left\{ \begin{array}{l} -A_{11}\dfrac{n}{R^2} - k_s A_{66}\dfrac{n}{R^2} + \left(\dfrac{A_{77}l^2 n}{4R^2}\right)(-m^2) \\[2mm] + \left(-\dfrac{A_{77}l^2(n^3+n)}{4R^4}\right) \end{array} \right\}$$

$$K_{33} = \left\{ \begin{array}{l} k_s A_{55}(-m^2) - k_s A_{66}\left(\dfrac{n}{R}\right)^2 - \dfrac{A_{11}}{R^2} - \dfrac{A_{77}l^2}{4}(m^4) + \\[2mm] \left(\dfrac{A_{77}l^2(2n^2+1)}{4R^2}\right)(-m^2) \\[2mm] \left(-\dfrac{A_{77}l^2(n^2+n^4)}{4R^4}\right) - N_h\dfrac{n^2}{R^2} \end{array} \right\}$$

$$K_{34} = \left\{ \begin{array}{l} k_s A_{66}(-m) - \dfrac{B_{12}}{R}(-m) + \dfrac{A_{77}l^2}{4}(m^3) \\[2mm] - \left(\dfrac{A_{77}l^2(n^2+1)}{4R^2}\right)(-m) \end{array} \right\}$$

$$K_{35} = \left\{ \begin{array}{l} \dfrac{k_s A_{55}n}{R} - \dfrac{B_{11}n}{R^2} + \left(\dfrac{B_{77}l^2 n}{2R^2} - \dfrac{A_{77}l^2 n}{4R}\right)(-m^2) \\[2mm] + \left(\dfrac{A_{77}l^2(n-n^3)}{4R^3}\right) \end{array} \right\}$$

$$K_{41} = \left\{ \begin{array}{l} +B_{11}(-m^2) - B_{66}\dfrac{n^2}{R^2} + \dfrac{B_{77}l^2 n^2}{4R^2}(-m^2) \\[2mm] + \left(\dfrac{5A_{77}l^2 n^2}{4R^3} - \dfrac{B_{77}l^2 n^4}{4R^4}\right) \end{array} \right\}$$

$$K_{42} = -\left\{ \begin{array}{l} -\dfrac{B_{66}n}{R}(m) - \dfrac{B_{12}n}{R}(m) - \dfrac{B_{77}l^2 n}{4R}(-m^3) \\[2mm] - \left(\dfrac{A_{77}l^2 n}{2R^2} + \dfrac{B_{77}l^2(-n^3+n)}{4R^3}\right)(m) \end{array} \right\}$$

$$K_{43} = -\left\{ \begin{array}{l} k_s A_{66}(m) - \dfrac{B_{12}}{R}(m) + \dfrac{A_{77}l^2}{4}(-m^3) \\[2mm] - \left(\dfrac{A_{77}l^2(n^2+1)}{4R^2}\right)(m) \end{array} \right\}$$

$$K_{44} = \left\{ \begin{array}{l} -D_{66}\left(\dfrac{n}{R}\right)^2 - k_s A_{66} + \left(\dfrac{D_{77}l^2 n^2}{4R^2} + \dfrac{A_{77}l^2}{4}\right)(-m^2) \\[2mm] + \left(-\dfrac{D_{77}l^2 n^4}{4R^4} + \dfrac{2B_{77}l^2 n^2}{4R^3} - \dfrac{A_{77}l^2(1+4n^2)}{4R^2}\right)D_{11}(-m^2) \end{array} \right\}$$

$$K_{45} = \left\{ \begin{array}{l} \dfrac{D_{12}n}{R}(m) + D_{66}\dfrac{n}{R}(m) + \dfrac{D_{77}l^2 n}{4R}(-m^3) \\[2mm] + \left(-\dfrac{D_{77}l^2 n^3}{4R^3} + \dfrac{B_{77}l^2 n}{2R} - \dfrac{3A_{77}l^2 n}{4R}\right)(m) \end{array} \right\}$$

$$K_{51} = \left\{ \begin{array}{l} +\dfrac{B_{12}n}{R}(-m) + \dfrac{B_{66}n}{R}(-m) + \dfrac{B_{77}l^2 n}{4R}\displaystyle\sum_{k=1}^{i} C_{i,k}^{(3)} \\[3mm] -\left(\dfrac{(B_{77})l^2 n}{2R^3} + \dfrac{A_{77}l^2 n}{4R^2} - \dfrac{B_{77}l^2 n^3}{4R^3}\right)(-m) \end{array} \right\}$$

$$K_{52} = \left\{ \begin{array}{l} B_{66}(-m^2) - B_{11}(\dfrac{n}{R})^2 + \dfrac{k_s A_{66}}{R} - \dfrac{B_{77}l^2}{4}(m^4) \\[3mm] -\left(\dfrac{-3A_{77}l^2}{4R} - \dfrac{B_{77}l^2}{2R} - \dfrac{B_{77}l^2(n^2-1)}{4R^2}\right)(-m^2) \\[3mm] +\left(\dfrac{A_{77}l^2(1-n^2)}{4R^3}\right) \end{array} \right\}$$

$$K_{53} = \left\{ \begin{array}{l} \dfrac{k_s A_{77}n}{R} - \dfrac{B_{11}n}{R^2} + \left(\dfrac{B_{77}l^2 n}{2R^2} - \dfrac{A_{77}l^2 n}{4R}\right)(-m^2) \\[3mm] +\left(\dfrac{A_{77}l^2(n-n^3)}{4R^3}\right) \end{array} \right\}$$

$$K_{54} = -\left\{ \begin{array}{l} +\dfrac{D_{12}n}{R}(-m) + D_{66}\dfrac{n}{R}(-m) + \dfrac{D_{77}l^2 n}{4R}(m^3) \\[3mm] +\left(-\dfrac{D_{77}l^2 n^3}{4R^3} + \dfrac{B_{77}l^2 n}{2R} - \dfrac{3A_{77}l^2 n}{4R}\right)(-m) \end{array} \right\}$$

$$K_{55} = \left\{ \begin{array}{l} -D_{11}(\dfrac{n}{R})^2 + D_{66}(-m^2) - k_s A_{55} - \dfrac{D_{77}l^2}{4}(m^4) \\[3mm] +\left(\dfrac{D_{77}l^2 n^2}{4R^2} + \dfrac{B_{77}l^2}{2R} + A_{77}l^2 + \dfrac{D_{77}l^2}{2R}\right)(-m^2) \\[3mm] +\left(-\dfrac{A_{77}l^2 n^2}{4R^2} - \dfrac{A_{77}l^2}{4R^2}\right) \end{array} \right\}$$

$M_{11} = I_0, M_{14} = I_1, M_{22} = I_0, M_{25} = I_1, M_{33} = I_0,$
$M_{41} = I_1, M_{44} = I_2, M_{52} = I_1, M_{55} = I_2$
$M_{12} = M_{13} = M_{15} = M_{21} = M_{23} = M_{24} = M_{31}$
$\quad = M_{32} = M_{34} = M_{35} = M_{42} = M_{43}$
$\quad = M_{45} = M_{51} = M_{53} = M_{54} = 0$

Appendix B

$$B_1 = \frac{1}{\Delta F}\begin{vmatrix} T_i & K_o(q(r_i)) \\ T_o & K_o(q(r_o)) \end{vmatrix} \quad C_1 = \frac{1}{\Delta F}\begin{vmatrix} I_o(q(r_i)) & T_i \\ I_o(q(r_o)) & T_o \end{vmatrix}$$

$$\Delta F = \begin{vmatrix} I_o(q(r_i)) & K_o(q(r_i)) \\ I_o(q(r_o)) & K_o(q(r_o)) \end{vmatrix}$$

FG-V:

$$A_1 = 1 - \frac{2D_z r_i}{h}, \ A_2 = \frac{2D_z}{h}, \ A_3 = P_m^2\left(\frac{2D_x r_i}{h} - 1\right),$$

$$A_4 = -2P_m^2\frac{D_x}{h}, \ \frac{k_i}{k_m} = 1 + 2D_i\left(\frac{z-r_i}{h}\right)$$

FG-X:

when: $z \langle \ r_i + \dfrac{h}{2}$ $A_1 = 1 + 2D_z\left(1 + \dfrac{2r_i}{h}\right),$

$$A_2 = -\frac{4D_z}{h}, \ A_3 = -P_m^2\left(1 + 2D_x\left(1 + \frac{2r_i}{h}\right)\right),$$

$$A_4 = 4P_m^2\frac{D_x}{h} \quad \frac{k_i}{k_m} = 1 + 2D_i\left(1 - \frac{2(z-r_i)}{h}\right)$$

when: $z \rangle r_i + \dfrac{h}{2}$ $A_1 = 1 - 2D_z\left(1 + \dfrac{2r_o}{h}\right),$

$$A_2 = \frac{4D_z}{h}, \ A_3 = -P_m^2\left(1 - 2D_x\left(1 + \frac{2r_o}{h}\right)\right),$$

$$A_4 = -4P_m^2\frac{D_x}{h} \quad \frac{k_i}{k_m} = 1 + 2D_i\left(-1 + \frac{2(z-r_i)}{h}\right)$$

FG-O:

when: $z\langle r_i + \dfrac{h}{2}$ $A_1 = 1 - \dfrac{4D_z r_i}{h},$

$$A_2 = \frac{4D_z}{h}, \ A_3 = P_m^2\left(\frac{4D_x r_i}{h} - 1\right),$$

$$A_4 = -4P_m^2\frac{D_x}{h} \quad \frac{k_i}{k_m} = 1 + 4D_i\left(\frac{z-r_i}{h}\right)$$

when: $z \rangle r_i + \dfrac{h}{2}$ $A_1 = 1 + \dfrac{4D_z r_o}{h},$

$$A_2 = -\frac{4D_z}{h}, \ A_3 = -P_m^2\left(\frac{4D_x r_o}{h} + 1\right),$$

$$A_4 = 4P_m^2\frac{D_x}{h} \quad \frac{k_i}{k_m} = 1 + 4D_i\left(\frac{r_o-z}{h}\right)$$

$$B_2 = \frac{1}{\displaystyle\int_{r_i}^{r_o} \frac{e^{2\sqrt{-\frac{A_4}{A_2}}\,z}}{z(A_2 z + A_1)H_z^2}dz}$$

$$\times \left\{ \frac{T_o}{H_o \times e^{-\sqrt{-\frac{A_4}{A_2}}\,r_o}} - \frac{T_i}{H_i \times e^{-\sqrt{-\frac{A_4}{A_2}}\,r_i}} \right\} \quad C_2 =$$

$$\frac{T_i}{HeunC\left(\frac{2A_1}{A_2}\sqrt{-\frac{A_4}{A_2}}, 0, 0, \frac{A_1}{A_2^3}\left(A_1 A_4 - A_2 A_3\right), 0, -\frac{A_2}{A_1}r_i\right) \times e^{-\sqrt{-\frac{A_4}{A_2}}\,r_i}}$$

$$H_z = HeunC\left(\frac{2A_1}{A_2}\sqrt{-\frac{A_4}{A_2}}, 0, 0, \frac{A_1}{A_2^3}(A_1A_4 - A_2A_3), 0, -\frac{A_2}{A_1}z \right)$$

$$H_o = HeunC\left(\frac{2A_1}{A_2}\sqrt{-\frac{A_4}{A_2}}, 0, 0, \frac{A_1}{A_2^3}(A_1A_4 - A_2A_3), 0, -\frac{A_2}{A_1}r_o \right)$$

$$H_i = HeunC\left(\frac{2A_1}{A_2}\sqrt{-\frac{A_4}{A_2}}, 0, 0, \frac{A_1}{A_2^3}(A_1A_4 - A_2A_3), 0, -\frac{A_2}{A_1}r_i \right)$$

$$B_3 = \frac{1}{\Delta A}\begin{vmatrix} T_2 & K_o(m_a z) \\ T_{ai} & K_o(m_a(r_o - h_p)) \end{vmatrix} \quad C_3 = \frac{1}{\Delta A}\begin{vmatrix} I_o(m_a z) & T_2 \\ I_o(m_a(r_o - h_p)) & T_{ai} \end{vmatrix}$$

$$\Delta A = \begin{vmatrix} I_o(m_a z) & K_o(m_a z) \\ I_o(m_a(r_o - h_p)) & K_o(m_a(r_o - h_p)) \end{vmatrix}$$

Where $T_{ai} = T_a|_{z=r_o-h_p}$

References

1. Zhao X, Li D, Yang B, Ma C, Zhu Y, Chen H (2014) Feature selection based on improved ant colony optimization for online detection of foreign fiber in cotton. Appl Soft Comput 24:585–596
2. Wang M, Chen H (2020) Chaotic multi-swarm whale optimizer boosted support vector machine for medical diagnosis. Appl Soft Comput 88:105946
3. Zhao X, Zhang X, Cai Z, Tian X, Wang X, Huang Y, Chen H, Hu L (2019) Chaos enhanced grey wolf optimization wrapped ELM for diagnosis of paraquat-poisoned patients. Comput Biol Chem 78:481–490
4. Xu X, Chen H-L (2014) Adaptive computational chemotaxis based on field in bacterial foraging optimization. Soft Comput 18(4):797–807
5. Shen L, Chen H, Yu Z, Kang W, Zhang B, Li H, Yang B, Liu D (2016) Evolving support vector machines using fruit fly optimization for medical data classification. Knowl Based Syst 96:61–75
6. Wang M, Chen H, Yang B, Zhao X, Hu L, Cai Z, Huang H, Tong C (2017) Toward an optimal kernel extreme learning machine using a chaotic moth-flame optimization strategy with applications in medical diagnoses. Neurocomputing 267:69–84
7. Xu Y, Chen H, Luo J, Zhang Q, Jiao S, Zhang X (2019) Enhanced Moth-flame optimizer with mutation strategy for global optimization. Inf Sci 492:181–203
8. Chen H, Zhang Q, Luo J, Xu Y, Zhang X (2020) An enhanced Bacterial Foraging Optimization and its application for training kernel extreme learning machine. Appl Soft Comput 86:105884
9. Cao L, Tu C, Hu P, Liu S (2019) Influence of solid particle erosion (SPE) on safety and economy of steam turbines. Appl Therm Eng 150:552–563
10. Wang Y, Cao L, Hu P, Li B, Li Y (2019) Model establishment and performance evaluation of a modified regenerative system for a 660 MW supercritical unit running at the IPT-setting mode. Energy 179:890–915
11. Zhu B, Zhou X, Liu X, Wang H, He K, Wang P (2020) Exploring the risk spillover effects among China's pilot carbon markets: a regular vine copula-CoES approach. J Clean Prod 242:118455
12. Liu X, Zhou X, Zhu B, He K, Wang P (2019) Measuring the maturity of carbon market in China: an entropy-based TOPSIS approach. J Clean Prod 229:94–103
13. Zhu B, Ye S, Jiang M, Wang P, Wu Z, Xie R, Chevallier J, Wei Y-M (2019) Achieving the carbon intensity target of China: a least squares support vector machine with mixture kernel function approach. Appl Energy 233:196–207
14. Zhu B, Su B, Li Y (2018) Input-output and structural decomposition analysis of India's carbon emissions and intensity, 2007/08–2013/14. Appl Energy 230:1545–1556
15. Cao Y, Li Y, Zhang G, Jermsittiparsert K, Nasseri M (2020) An efficient terminal voltage control for PEMFC based on an improved version of whale optimization algorithm. Energy Rep 6:530–542
16. Liu Y-X, Yang C-N, Sun Q-D, Wu S-Y, Lin S-S, Chou Y-S (2019) Enhanced embedding capacity for the SMSD-based data-hiding method. Signal Process Image Commun 78:216–222
17. Quan Q, Hao Z, Xifeng H, Jingchun L (2020) Research on water temperature prediction based on improved support vector regression. Neural Comput Appl. https://doi.org/10.1007/s00521-020-04836-4
18. Shi G, Araby S, Gibson CT, Meng Q, Zhu S, Ma J (2018) Graphene platelets and their polymer composites: fabrication, structure, properties, and applications. Adv Func Mater 28(19):1706705
19. Chen S, Hassanzadeh-Aghdam M, Ansari R (2018) An analytical model for elastic modulus calculation of SiC whisker-reinforced hybrid metal matrix nanocomposite containing SiC nanoparticles. J Alloy Compd 767:632–641
20. Zhang X, Zhang Y, Liu Z, Liu J (2020) Analysis of heat transfer and flow characteristics in typical cambered ducts. Int J Therm Sci 150:106226
21. Hu X, Ma P, Wang J, Tan G (2019) A hybrid cascaded DC–DC boost converter with ripple reduction and large conversion ratio. IEEE J Emerg Sel Topics Power Electron 8(1):761–770
22. Hu X, Ma P, Gao B, Zhang M (2019) An integrated step-up inverter without transformer and leakage current for grid-connected photovoltaic system. IEEE Trans Power Electron 34(10):9814–9827
23. Wu X, Huang B, Wang Q, Wang Y (2020) High energy density of two-dimensional MXene/NiCo-LDHs interstratification assembly electrode: Understanding the role of interlayer ions and hydration. Chem Eng J 380:122456
24. Guo L, Sriyakul T, Nojavan S, Jermsittiparsert K (2020) Risk-based traded demand response between consumers' aggregator and retailer using downside risk constraints technique. IEEE Access 8:90957–90968
25. Cao B, Zhao J, Lv Z, Gu Y, Yang P, Halgamuge SK (2020) Multiobjective evolution of fuzzy rough neural network via distributed parallelism for stock prediction. IEEE Trans Fuzzy Syst 28(5):939–952
26. Wang G, Yao Y, Chen Z, Hu P (2019) Thermodynamic and optical analyses of a hybrid solar CPV/T system with high solar concentrating uniformity based on spectral beam splitting technology. Energy 166:256–266
27. Liu Y, Yang C, Sun Q (2020) Thresholds based image extraction schemes in big data environment in intelligent traffic management. IEEE Transact Intell Transport Syst. https://doi.org/10.1109/TITS.2020.2994386
28. Liu J, Liu Y, Wang X (2019) An environmental assessment model of construction and demolition waste based on system dynamics: a case study in Guangzhou. Environ Sci Pollut Res. https://doi.org/10.1007/s11356-019-07107-5
29. Xu W, Qu S, Zhao L, Zhang H (2020) An improved adaptive sliding mode observer for a middle and high-speed rotors tracking. IEEE Transact Power Electron. https://doi.org/10.1109/TPEL.2020.3000785

30. Rafiee MA, Rafiee J, Wang Z, Song H, Yu Z-Z, Koratkar N (2009) Enhanced mechanical properties of nanocomposites at low graphene content. ACS Nano 3(12):3884–3890

31. Yavari F, Rafiee M, Rafiee J, Yu Z-Z, Koratkar N (2010) Dramatic increase in fatigue life in hierarchical graphene composites. ACS Appl Mater Interfaces 2(10):2738–2743

32. Jafari M, Moradi G, Shirazi RS, Mirzavand R (2017) Design and implementation of a six-port junction based on substrate integrated waveguide. Turk J Electr Eng Comput Sci 25(3):2547–2553

33. Nadri S, Xie L, Jafari M, Bauwens MF, Arsenovic A, Weikle RM (2019) Measurement and extraction of parasitic parameters of quasi-vertical schottky diodes at submillimeter wavelengths. IEEE Microwave Wirel Compon Lett 29(7):474–476

34. Nadri S, Xie L, Jafari M, Alijabbari N, Cyberey ME, Barker NS, Lichtenberger AW, Weikle RM (2018) A 160 GHz frequency Quadrupler based on heterogeneous integration of GaAs Schottky diodes onto silicon using SU-8 for epitaxy transfer. In: 2018 IEEE/MTT-S international microwave symposium-IMS. IEEE, pp 769–772

35. Weikle RM, Xie L, Nadri S, Jafari M, Moore CM, Alijabbari N, Cyberey ME, Barker NS, Lichtenberger AW, Brown CL (2019) Submillimeter-wave schottky diodes based on heterogeneous integration of GaAs onto silicon. In: 2019 United States national committee of URSI national radio science meeting (USNC-URSI NRSM), IEEE, pp 1–2

36. Eyvazian A, Hamouda AM, Tarlochan F, Mohsenizadeh S, Dastjerdi AA (2019) Damping and vibration response of viscoelastic smart sandwich plate reinforced with non-uniform Graphene platelet with magnetorheological fluid core. Steel Compos Struct 33(6):891

37. Motezaker M, Eyvazian A (2020) Post-buckling analysis of Mindlin Cut out-plate reinforced by FG-CNTs. Steel Compos Struct 34(2):289

38. Motezaker M, Eyvazian A (2020) Buckling load optimization of beam reinforced by nanoparticles. Struct Eng Mech 73(5):481–486

39. Derazkola HA, Eyvazian A, Simchi A (2020) Modeling and experimental validation of material flow during FSW of polycarbonate. Mater Today Commun 22:100796

40. Eyvazian A, Hamouda A, Tarlochan F, Derazkola HA, Khodabakhshi F (2020) Simulation and experimental study of underwater dissimilar friction-stir welding between aluminium and steel. J Mater Res Technol. https://doi.org/10.1016/j.jmrt.2020.02.003

41. Eyvazian A, Habibi MK, Hamouda AM, Hedayati R (2014) Axial crushing behavior and energy absorption efficiency of corrugated tubes. Mater Des 1980–2015(54):1028–1038

42. Feng C, Kitipornchai S, Yang J (2017) Nonlinear bending of polymer nanocomposite beams reinforced with non-uniformly distributed graphene platelets (GPLs). Compos B Eng 110:132–140

43. Čanadija M, Barretta R, De Sciarra FM (2016) A gradient elasticity model of Bernoulli-Euler nanobeams in non-isothermal environments. Europ J Mech A/Solids 55:243–255

44. Barretta R, Brčić M, Čanadija M, Luciano R, de Sciarra FM (2017) Application of gradient elasticity to armchair carbon nanotubes: Size effects and constitutive parameters assessment. Europ J Mech A/Solids 65:1–13

45. Barretta R, Čanadija M, Feo L, Luciano R, de Sciarra FM, Penna R (2018) Exact solutions of inflected functionally graded nanobeams in integral elasticity. Compos B Eng 142:273–286

46. Qu S, Zhao L, Xiong Z (2020) Cross-layer congestion control of wireless sensor networks based on fuzzy sliding mode control. Neural Comput Appl. https://doi.org/10.1007/s00521-020-04758-1

47. Zhang H, Qu S, Li H, Luo J, Xu W (2020) A moving shadow elimination method based on fusion of multi-feature. IEEE Access 8:63971–63982

48. Pang R, Xu B, Kong X, Zou D (2018) Seismic fragility for high CFRDs based on deformation and damage index through incremental dynamic analysis. Soil Dyn Earthq Eng 104:432–436

49. Pang R, Xu B, Zhou Y, Zhang X, Wang X (2020) Fragility analysis of high CFRDs subjected to mainshock-aftershock sequences based on plastic failure. Eng Struct 206:110152

50. Guo J, Zhang X, Gu F, Zhang H, Fan Y (2020) Does air pollution stimulate electric vehicle sales? Empirical evidence from twenty major cities in China. J Clean Prod 249:119372

51. Zeng H-B, Teo KL, He Y, Wang W (2019) Sampled-data-based dissipative control of TS fuzzy systems. Appl Math Model 65:415–427

52. Gao N-S, Guo X-Y, Cheng B-Z, Zhang Y-N, Wei Z-Y, Hou H (2019) Elastic wave modulation in hollow metamaterial beam with acoustic black hole. IEEE Access 7:124141–124146

53. Chen H, Zhang G, Fan D, Fang L, Huang L (2020) Nonlinear lamb wave analysis for microdefect identification in mechanical structural health assessment. Measurement. https://doi.org/10.1016/j.measurement.2020.108026

54. Gao N, Wei Z, Hou H, Krushynska AO (2019) Design and experimental investigation of V-folded beams with acoustic black hole indentations. J Acoust Soc Am 145(1):EL79–EL83

55. Song Q, Zhao H, Jia J, Yang L, Lv W, Gu Q, Shu X (2020) Effects of demineralization on the surface morphology, microcrystalline and thermal transformation characteristics of coal. J Anal Appl Pyrol 145:104716

56. Sahmani S, Aghdam M (2017) A nonlocal strain gradient hyperbolic shear deformable shell model for radial postbuckling analysis of functionally graded multilayer GPLRC nanoshells. Compos Struct 178:97–109

57. Sahmani S, Aghdam M (2017) Nonlinear instability of axially loaded functionally graded multilayer graphene platelet-reinforced nanoshells based on nonlocal strain gradient elasticity theory. Int J Mech Sci 131:95–106

58. Mirsalehi M, Azhari M, Amoushahi H (2017) Buckling and free vibration of the FGM thin micro-plate based on the modified strain gradient theory and the spline finite strip method. Europ J Mech A/Solids 61:1–13

59. Song M, Kitipornchai S, Yang J (2017) Free and forced vibrations of functionally graded polymer composite plates reinforced with graphene nanoplatelets. Compos Struct 159:579–588

60. Atanasov MS, Karličić D, Kozić P (2017) Forced transverse vibrations of an elastically connected nonlocal orthotropic double-nanoplate system subjected to an in-plane magnetic field. Acta Mech 228(6):2165–2185

61. Du C, Li Y, Jin X (2014) Nonlinear forced vibration of functionally graded cylindrical thin shells. Thin Walled Struct 78:26–36

62. Li X, Qin Y, Li Y, Zhao X (2018) The coupled vibration characteristics of a spinning and axially moving composite thin-walled beam. Mech Adv Mater Struct 25(9):722–731

63. Barati MR (2018) A general nonlocal stress-strain gradient theory for forced vibration analysis of heterogeneous porous nanoplates. Europ J Mech A/Solids 67:215–230

64. Chen D, Yang J, Kitipornchai S (2016) Free and forced vibrations of shear deformable functionally graded porous beams. Int J Mech Sci 108:14–22

65. Chen D, Kitipornchai S, Yang J (2016) Nonlinear free vibration of shear deformable sandwich beam with a functionally graded porous core. Thin Walled Struct 107:39–48

66. Chen D, Yang J, Kitipornchai S (2017) Nonlinear vibration and postbuckling of functionally graded graphene reinforced porous nanocomposite beams. Compos Sci Technol 142:235–245

67. Dong Y, Li Y, Chen D, Yang J (2018) Vibration characteristics of functionally graded graphene reinforced porous nanocomposite cylindrical shells with spinning motion. Compos B Eng 145:1–13

68. Yang J, Chen D, Kitipornchai S (2018) Buckling and free vibration analyses of functionally graded graphene reinforced porous nanocomposite plates based on Chebyshev-Ritz method. Compos Struct 193:281–294

69. Chen D, Kitipornchai S, Yang J (2018) Dynamic response and energy absorption of functionally graded porous structures. Mater Des 140:473–487

70. Li X, Li Y, Qin Y (2016) Free vibration characteristics of a spinning composite thin-walled beam under hygrothermal environment. Int J Mech Sci 119:253–265

71. Li X, Du C, Li Y (2018) Parametric instability of a functionally graded cylindrical thin shell subjected to both axial disturbance and thermal environment. Thin Walled Struct 123:25–35

72. Li X, Du C, Li Y (2018) Parametric resonance of a FG cylindrical thin shell with periodic rotating angular speeds in thermal environment. Appl Math Model 59:393–409

73. Du C, Li Y (2013) Nonlinear resonance behavior of functionally graded cylindrical shells in thermal environments. Compos Struct 102:164–174

74. Du C, Li Y (2014) Nonlinear internal resonance of functionally graded cylindrical shells using the Hamiltonian dynamics. Acta Mech Solida Sin 27(6):635–647

75. Moayedi H, Hayati S (2018) Modelling and optimization of ultimate bearing capacity of strip footing near a slope by soft computing methods. Appl Soft Comput J 66:208–219. https://doi.org/10.1016/j.asoc.2018.02.027

76. Moayedi H, Hayati S (2018) Applicability of a CPT-based neural network solution in predicting load-settlement responses of bored pile. Int J Geomech. https://doi.org/10.1061/(ASCE)GM.1943-5622.0001125

77. Moayedi H, Aghel B, Abdullahi MM, Nguyen H, Safuan A, Rashid A (2019) Applications of rice husk ash as green and sustainable biomass. J Clean Prod. https://doi.org/10.1016/j.jclepro.2019.117851

78. Moayedi H, Bui DT, Foong LK (2019) Slope stability monitoring using novel remote sensing based fuzzy logic. Sensors (Switzerland). https://doi.org/10.3390/s19214636

79. Moayedi H, Bui DT, Gör M, Pradhan B, Jaafari A (2019) The feasibility of three prediction techniques of the artificial neural network, adaptive neuro-fuzzy inference system, and hybrid particle swarm optimization for assessing the safety factor of cohesive slopes. ISPRS Int J Geo Inf. https://doi.org/10.3390/ijgi8090391

80. Moayedi H, Bui DT, Kalantar B, Osouli A, Gör M, Pradhan B, Nguyen H, Rashid ASA (2019) Harris hawks optimization: A novel swarm intelligence technique for spatial assessment of landslide susceptibility. Sensors (Switzerland). https://doi.org/10.3390/s19163590

81. Moayedi H, Hayati S (2019) Artificial intelligence design charts for predicting friction capacity of driven pile in clay. Neural Comput Appl 31(11):7429–7445. https://doi.org/10.1007/s00521-018-3555-5

82. Moayedi H, Mu'azu MA, Kok Foong L (2019) Swarm-based analysis through social behavior of grey wolf optimization and genetic programming to predict friction capacity of driven piles. Eng Comput. https://doi.org/10.1007/s00366-019-00885-z

83. Moayedi H, Nguyen H, Kok Foong L (2019) Nonlinear evolutionary swarm intelligence of grasshopper optimization algorithm and gray wolf optimization for weight adjustment of neural network. Eng Comput. https://doi.org/10.1007/s00366-019-00882-2

84. Moayedi H, Osouli A, Nguyen H, Rashid ASA (2019) A novel Harris hawks' optimization and k-fold cross-validation predicting

85. slope stability. Eng Comput. https://doi.org/10.1007/s00366-019-00828-8

86. Moayedi H, Rezaei A (2019) An artificial neural network approach for under-reamed piles subjected to uplift forces in dry sand. Neural Comput Appl 31(2):327–336. https://doi.org/10.1007/s00521-017-2990-z

87. Yuan C, Moayedi H (2019) The performance of six neural-evolutionary classification techniques combined with multi-layer perception in two-layered cohesive slope stability analysis and failure recognition. Eng Comput. https://doi.org/10.1007/s00366-019-00791-4

88. Yuan C, Moayedi H (2019) Evaluation and comparison of the advanced metaheuristic and conventional machine learning methods for the prediction of landslide occurrence. Eng Comput. https://doi.org/10.1007/s00366-019-00798-x

89. Moayedi H, Aghel B, Vaferi B, Foong LK, Bui DT (2020) The feasibility of Levenberg–Marquardt algorithm combined with imperialist competitive computational method predicting drag reduction in crude oil pipelines. J Petrol Sci Eng. https://doi.org/10.1016/j.petrol.2019.106634

90. Moayedi H, Moatamediyan A, Nguyen H, Bui XN, Bui DT, Rashid ASA (2020) Prediction of ultimate bearing capacity through various novel evolutionary and neural network models. Eng Comput 36(2):671–687. https://doi.org/10.1007/s00366-019-00723-2

91. Al-Furjan M, Safarpour H, Habibi M, Safarpour M, Tounsi A (2020) A comprehensive computational approach for nonlinear thermal instability of the electrically FG-GPLRC disk based on GDQ method. Eng Comput. https://doi.org/10.1007/s00366-020-01088-7

92. Shi X, Li J, Habibi M (2020) On the statics and dynamics of an electro-thermo-mechanically porous GPLRC nanoshell conveying fluid flow. Mech Based Des Struct Mach 1–37

93. Shamsaddini Lori E, Ebrahimi F, Elianddy Bin Supeni E, Habibi M, Safarpour H (2020) The critical voltage of a GPL-reinforced composite microdisk covered with piezoelectric layer. Eng Comput. https://doi.org/10.1007/s00366-020-01004-z

94. Ghabussi A, Habibi M, NoormohammadiArani O, Shavalipour A, Moayedi H, Safarpour H (2020) Frequency characteristics of a viscoelastic graphene nanoplatelet–reinforced composite circular microplate. J Vib Control. https://doi.org/10.1177/1077546320923930

95. Adamian A, Safari KH, Sheikholeslami M, Habibi M, Al-Furjan M, Chen G (2020) Critical temperature and frequency characteristics of GPLs-reinforced composite doubly curved panel. Appl Sci 10(9):3251

96. Shariati A, Ghabussi A, Habibi M, Safarpour H, Safarpour M, Tounsi A, Safa M (2020) Extremely large oscillation and nonlinear frequency of a multi-scale hybrid disk resting on nonlinear elastic foundation. Thin Walled Struct 154:106840

97. Shariati A, Habibi M, Tounsi A, Safarpour H, Safa M Application of exact continuum size-dependent theory for stability and frequency analysis of a curved cantilevered microtubule by considering viscoelastic properties. https://doi.org/10.1007/s00366-020-01024-9

98. Habibi M, Safarpour M, Safarpour H (2020) Vibrational characteristics of a FG-GPLRC viscoelastic thick annular plate using fourth-order Runge-Kutta and GDQ methods. Mech Based Des Struct Mach. https://doi.org/10.1080/15397734.2020.1779086

99. Oyarhossein MA, Aa A, Habibi M, Makkiabadi M, Daman M, Safarpour H, Jung DW (2020) Dynamic response of the nonlocal strain-stress gradient in laminated polymer composites microtubes. Sci Rep 10(1):5616. https://doi.org/10.1038/s41598-020-61855-w

100. Moayedi H, Ebrahimi F, Habibi M, Safarpour H, Foong LK (2020) Application of nonlocal strain–stress gradient theory and

GDQEM for thermo-vibration responses of a laminated composite nanoshell. Eng Comput. https://doi.org/10.1007/s00366-020-01002-1

100. Cheshmeh E, Karbon M, Eyvazian A, Jung D, Tran T, Habibi M, Safarpour M (2020) Buckling and vibration analysis of FG-CNTRC plate subjected to thermo-mechanical load based on higher-order shear deformation theory. Mech Based Des Struct Mach. https://doi.org/10.1080/15397734.2020.1744005

101. Moayedi H, Aliakbarlou H, Jebeli M, Noormohammadi Arani O, Habibi M, Safarpour H, Foong L (2020) Thermal buckling responses of a graphene reinforced composite micropanel structure. Int J Appl Mech. https://doi.org/10.1142/S1758825120500106

102. Ebrahimi F, Supeni EEB, Habibi M, Safarpour H (2020) Frequency characteristics of a GPL-reinforced composite microdisk coupled with a piezoelectric layer. Europ Phys J Plus 135(2):144

103. Najaafi N, Jamali M, Habibi M, Sadeghi S, Jung DW, Nabipour N (2020) Dynamic instability responses of the substructure living biological cells in the cytoplasm environment using stress-strain size-dependent theory. J Biomol Struct Dyn. https://doi.org/10.1080/07391102.2020.1751297

104. Sahmani S, Aghdam MM, Rabczuk T (2018) Nonlocal strain gradient plate model for nonlinear large-amplitude vibrations of functionally graded porous micro/nano-plates reinforced with GPLs. Compos Struct 198:51–62

105. Liu W, Zhang X, Li H, Chen J (2020) Investigation on the deformation and strength characteristics of rock salt under different confining pressures. Geotech Geol Eng. https://doi.org/10.1007/s10706-020-01388-1

106. Fazaeli A, Habibi M, Ekrami A (2016) Experimental and finite element comparison of mechanical properties and formability of dual phase steel and ferrite-pearlite steel with the same chemical composition. Metall Eng 19(2):84–93

107. Ghazanfari A, Soleimani SS, Keshavarzzadeh M, Habibi M, Assempuor A, Hashemi R (2019) Prediction of FLD for sheet metal by considering through-thickness shear stresses. Mech Based Des Struct Mach. https://doi.org/10.1080/15397734.2019.1662310

108. Habibi M, Mohammadi A, Safarpour H, Shavalipour A, Ghadiri M (2019) Wave propagation analysis of the laminated cylindrical nanoshell coupled with a piezoelectric actuator. Mech Based Des Struct Mach. https://doi.org/10.1080/15397734.2019.1697932

109. Habibi M, Payganeh G (2018) Experimental and finite element investigation of titanium tubes hot gas forming and production of square cross-section specimens.

110. Shokrgozar A, Safarpour H, Habibi M (2020) Influence of system parameters on buckling and frequency analysis of a spinning cantilever cylindrical 3D shell coupled with piezoelectric actuator. Proc Inst Mech Eng Part C J Mech Eng Sci 234(2):512–529

111. Shariati A, Mohammad-Sedighi H, Żur KK, Habibi M, Safa M (2020) On the vibrations and stability of moving viscoelastic axially functionally graded nanobeams. Materials 13(7):1707

112. Zhang X, Shamsodin M, Wang H, NoormohammadiArani O, Khan AM, Habibi M, Al-Furjan M, (2020) Dynamic information of the time-dependent tobullian biomolecular structure using a high-accuracy size-dependent theory. J Biomol Struct Dyn. https://doi.org/10.1080/07391102.2020.1760939

113. Shokrgozar A, Ghabussi A, Ebrahimi F, Habibi M, Safarpour H (2020) Viscoelastic dynamics and static responses of a graphene nanoplatelets-reinforced composite cylindrical microshell.

Mech Based Des Struct Mach. https://doi.org/10.1080/15397734.2020.1719509

114. Moayedi H, Habibi M, Safarpour H, Safarpour M, Foong L (2019) Buckling and frequency responses of a graphen nanoplatelet reinforced composite microdisk. Int J Appl Mech. https://doi.org/10.1142/S1758825119501023

115. Mahdi Alipour S, Mohammadi K, Mohammadi A, Habibi M, Safarpour H (2019) On dynamic of electro-elastic GNPRC cylindrical shell using modified length-couple stress parameter. Mech Based Des Struct Mach. https://doi.org/10.1142/S1758825120500660

116. Shariati A, Mohammad-Sedighi H, Żur KK, Habibi M, Safa M (2020) Stability and dynamics of viscoelastic moving rayleigh beams with an asymmetrical distribution of material parameters. Symmetry 12(4):586

117. Jermsittiparsert K, Ghabussi A, Forooghi A, Shavalipour A, Habibi M, won Jung D, Safa M (2020) Critical voltage, thermal buckling and frequency characteristics of a thermally affected GPL reinforced composite microdisk covered with piezoelectric actuator. Mech Based Des Struct Mach. https://doi.org/10.1080/15397734.2020.1748052

118. Safarpour M, Ghabussi A, Ebrahimi F, Habibi M, Safarpour H (2020) Frequency characteristics of FG-GPLRC viscoelastic thick annular plate with the aid of GDQM. Thin Walled Struct 150:106683

119. Moayedi H, Darabi R, Ghabussi A, Habibi M, Foong LK (2020) Weld orientation effects on the formability of tailor welded thin steel sheets. Thin Walled Struct 149:106669

120. Safarpour M, Ebrahimi F, Habibi M, Safarpour H (2020) On the nonlinear dynamics of a multi-scale hybrid nanocomposite disk. Eng Comput. https://doi.org/10.1007/s00366-020-00949-5

121. Ghayesh MH (2019) Viscoelastic mechanics of Timoshenko functionally graded imperfect microbeams. Compos Struct 225:110974

122. Ghayesh MH (2018) Dynamics of functionally graded viscoelastic microbeams. Int J Eng Sci 124:115–131

123. Ghayesh MH (2019) Nonlinear oscillations of FG cantilevers. Appl Acoust 145:393–398

124. Ghayesh MH (2018) Nonlinear vibration analysis of axially functionally graded shear-deformable tapered beams. Appl Math Model 59:583–596

125. Ghayesh MH (2019) Dynamical analysis of multilayered cantilevers. Commun Nonlinear Sci Numer Simul 71:244–253

126. Ghayesh MH (2019) Asymmetric viscoelastic nonlinear vibrations of imperfect AFG beams. Appl Acoust 154:121–128

127. Tadi Beni Y, Mehralian F, Zeighampour H (2016) The modified couple stress functionally graded cylindrical thin shell formulation. Mech Adv Mater Struct 23(7):791–801

128. Ansari R, Gholami R, Rouhi H (2012) Vibration analysis of single-walled carbon nanotubes using different gradient elasticity theories. Compos B Eng 43(8):2985–2989

129. Wu H, Kitipornchai S, Yang J (2017) Thermal buckling and post-buckling of functionally graded graphene nanocomposite plates. Mater Des 132:430–441